Pulsatile Flow Interaction with a Stented Artery: Compliance Mismatch Effects

Liling Tang

Supervised by Dr. Ferchichi Mohsen

Date: 13th April 2007

A Thesis Submitted In Partial Fulfillment Of The Requirements
Of The MScEngi Degree In Control Engineering

Faculty of Engineering

Lakehead University

Thunder Bay, Ontario

Your file Votre référence
ISBN: 978-0-494-31840-9
Our file Notre référence
ISBN: 978-0-494-31840-9

Abstract

Atherosclerosis is a group of diseases characterized by thickening of the arterial wall resulting in a reduction in the cross-sectional area of the lumen. One of treatments for these artery diseases is stent angioplasty. In general, the stent has the role of supporting the arterial wall for increase blood flow areas. It is believed that this compliance mismatch affects both the vessel hemodynamics and wall mechanics.

To investigate the effects of compliance mismatch on blood flow in a nonlinear artery/stent system in the hope of achieving a better understanding of the influence of the artery/stent wall elasticity and geometric parameters on haemodynamics and wall mechanics of stented vessel, a fully coupled fluid-structure interaction analysis of pulsatile blood flow in a simplified model (an axisymmetric thin tube) is presented in this study. The flow, assumed incompressible and Newtonian, was driven by a pulsatile pressure at the artery inlet and a constant pressure at the outlet. The Navier-Stokes equations are used as the governing equations for the fluid flow. The simulations employ the commercial software ADINA (Automatic Dynamic Incremental Nonlinear Analysis) which is a fully coupled fluid-structure interaction finite element analysis package. Two stent geometries were investigated. In the first case, the stent had the same wall thickness as the artery and, in the second case the stent wall thickness was increased such that the flow area within the stent was smaller than that of the artery. To obtain a better understanding of pulsatile flow in stented arteries, a natural continuation of this study will be an experimental study.

Acknowledgement

I would like to express my sincere thanks and appreciation to my supervisor, Dr. M. Ferchichi for his support and guidance during my graduate studies. I would like to thank my co-supervisor Dr. A. Tayebi for his encouragement throughout the program. Also I would like to thank Mr. Joe Ripku for his assistance with my experimental work.

I dedicate this work to my parents Mr. & Mrs. Tang, my son Kevin Liu, and my husband Kefu Liu for their love, guidance and support.

Table of contents

List of figures

Symbols

ADINA	Automatic Dynamic Incremental Nonlinear Analysis
ALE	Arbitrary Lagrangian Eulerian
c_i, D_i	material constants
D_0	diameter of the tube
$\mathbf{d}$	displacement vector of the structure
E_a	Young's modulus of the artery
E_s	Young's modulus of the stented artery
FSI	Fluid-Structure Interaction
$\mathbf{f}_f^B$	body force vector of the fluid medium
$\mathbf{f}_s^B$	body force vector per unit volume
h	artery thickness
hs	stent thickness
I_1, I_2	invariants of the deformation tensor
ℓ	characteristic length
l, l_0	current fiber length and original length
Le	entrance length
Lo	outlet length
Ls	stent length
p_1	inlet pressure of the tube

p_2	outlet pressure of the tube
p_{ij}	local hydrostatic pressure
R_e	Reynolds number
S_t	Strouhal number
$\bar{U}$	entrance average velocity for the fully developed flow
u	fluid velocity
$\mathbf{u}$	fluid velocity vector
W	strain-energy density function

Greek symbols

α	Wormersley number
δ_{ij}	Kronecker delta
ε_{ij}	Green-Lagrange strains
λ and μ	Lame constants of the media
μ_f	dynamic fluid viscosity
ν	kinematic fluid viscosity
ρ_f	fluid density
ρ_s	mass density of the structure
σ	structure stress tensor
τ_p	wall principal stress
τ_w	shear stress
ω	pulsation frequency

Chapter 1 Introduction

Stroke and ischemic heart disease (a decrease in the blood supply to a bodily organ, tissue, or part caused by constriction or obstruction of the blood vessels) are one of the leading causes of death in the world. They are often related to arterial sclerosis (a thickening or hardening of a body part, as of an artery, especially from excessive formation of fibrous interstitial tissue), in particular, to the deposition of fat, cholesterol, calcium and fibrin at the inner wall of artery. The deposits, called atherosclerotic plaque would accumulate and slowly become thicker, reduce the cross-section of the arterial lumen. This condition is referred to as arterial stenosis (a constriction or narrowing of a duct or passage) and shown in Figure 1.1. High grade stenosis influences the dynamics of blood flow, in that it increases the flow resistance in arteries and potentially may lead to stroke and heart attack.

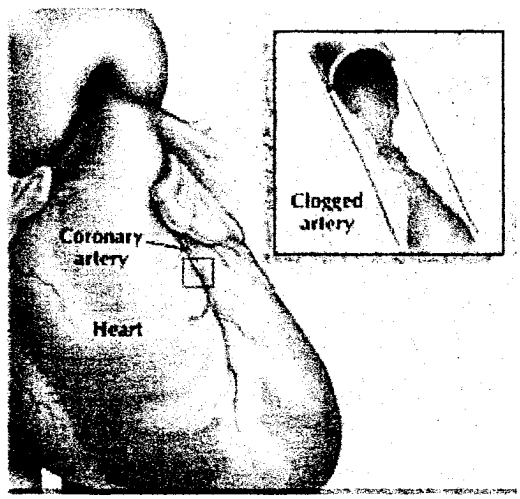

Figure 1.1: Stenotic artery[1]

[1] www.Harthosp.org

One of the medical interventions to heart stenosis is stent angioplasty (a medical procedure in which a balloon is used to open narrowed or blocked blood vessels of the heart) shown in Figure 1.2. A stent is a surgically implanted endovascular prosthetic device which acts to scaffold a blood vessel permanently open and compresses any lesions protruding into the vessel lumen. Such a treatment would improve blood flow to the heart muscle and relieves symptoms (usually chest pain). In general, the stent has the role of supporting the arterial wall also after the catheter retrieval. The procedure of implanting a stent in a stenotic artery is as follows: (1) catheter is threaded through a blood vessel in the groin and into the narrowed section of the heart artery. (2) A balloon is inflated, causing stent to expand. (3) The stent locks in place, propping the artery open. Then the balloon is deflated and the catheter is removed.

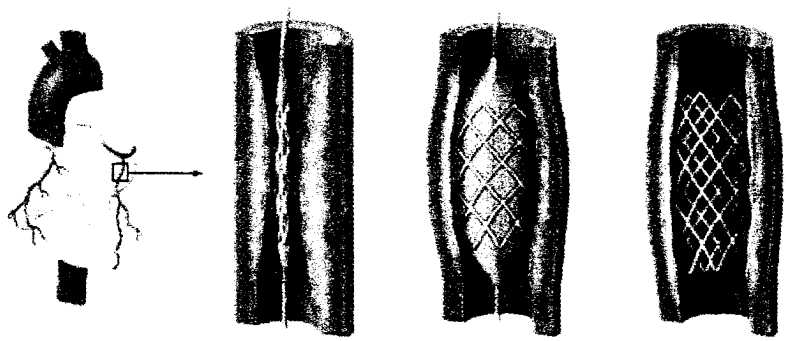

Figure 1.2: The procedure of implanting a stent in a stenotic artery[2]

It has been found however, that 20-50% of patients treated by the stent angioplasty developed a reoccurrence of stenosis at the site treated within 6 months (Grewe et al. 2000). This phenomenon, referred to as in-stent restenosis is believed to be due to thrombus deposition with recruitment of inflammatory cells to the stent struts and between the struts. Recently, various studies have shown that both the geometry of the

[2] www.thecardiologist.co.uk and www.uthsca.edu/mission/spring98/stent.html

stent and the level of intrusions into the blood vessel are responsible for the formation of a "non-smooth" section of the blood vessel. It is suggested that local flow of blood is adversely affected by this disturbance. The resulting variations of blood shear rate, wall shear stress, and formation of vortices are thought to be factors influencing the process of thrombus formation.

The rest of this chapter is organized as follows. Section 1.1 is a review of the previous studies on stenotic arteries and, hemodynamics and wall mechanics of stented arteries. The objectives of the present work will by outlined in Section 1.2.

1.1 Literature review

1.1.1 Stenotic arteries

Hardening of the arteries from atherosclerosis can produce high grade stenosis which leads to morbid symptoms of heart attack and stroke. Blood flow through the stenosis produces a low pressure zone at the throat which may cause the elastic artery to collapse. With a reduction of lumen due to stenosis, blood flow velocity increases. The high blood velocity in turn creates a low or negative transmural pressure, which can result in collapse of the artery. Alternatively the high velocities at the stenosis also cause high shear stresses, which may be related to plaque cap rupture.

A large volume of experimental and computational works have been conducted on the flow dynamics in stenotic elastic tubes over the years. Deplano and Siouffi (1999) conducted experimental and numerical study of pulsatile flow through stenosis: wall shear stress analysis. They demonstrated compressive wall stress, negative flow pressure, and high flow shear stress at the stenosis site. Their results showed that critical stress/strain conditions are very sensitive to changes in blood pressure conditions and material properties. A small change in stenosis severity leads to considerable changes of flow velocity, shear stress and pressure in the stenotic region, which in turn affects artery deformation.

Bathe and Kamm (1999) introduced an axisymmetric thick-wall model with fluid-structure interactions for pulsatile blood flow through a compliant stenotic artery. Their flow simulation was done using a commercially available finite element analysis system (Automatic Dynamic Incremental Nonlinear Analysis: ADINA) to solve the problem. The effect of increasing area reduction on fluid dynamic and structural stresses was studied and found that pressure drop, peak wall shear stress, and maximal principal stress in the lesion increase dramatically as the area reduction in the stenosis is increased from 51 to 89 percent. ADINA was also used to investigate hemodynamics in stenotic arteries. Tang et al. (1999) modeled a stenotic artery as a three-dimensional (3-D) thick-wall that included the effects of fluid-structure interaction (FSI). Furthermore, they extended their work by modeling a 3-D thin wall model (Tang, et al., 1999). A nonlinear axisymmetric model with fluid-wall interactions for steady viscous flow in stenotic elastic tubes was studied (Tang, et al., 1999). All these studies revealed that severe stenosis causes critical flow conditions as negative pressure and high and low shear stresses, which may relate to artery compressive, plaque cap rupture, platelet activation, and thrombus formation. In Ref. (Tang, et al., 2002), a 3-D nonlinear model with FSI was used to study unsteady viscous flow in stenotic tubes with cyclic wall collapse simulating blood flow in stenotic cartid arteries. The study found that there exist cyclic wall compression and collapse under physiological pressure conditions and stenosis severity and pressure condition are the dominating factors affecting wall compression and collapse. In Tang et al. (2004), effect of a lipid pool on stress/strain distributions in stenotic arteries was studied. The results indicated that critical plaque stress/strain conditions are very sensitive to changes in pressure conditions, material properties, plaque structure, lipid pool size, shape and position, and various model assumptions (axial stretch, radial expansion, FSI. Their results indicate that initial pressurization brings the biggest change (13 times higher) in maximum stress value compared to that in non-pressurized tube. Fluid-structure interactions affect extreme stress values (both positive and negative) in the 30%-50% range. A 36.5% axial stretch reduced the maximum value of the maximum principal stress by 20%, maximum compressive stress by 60%. A 50% increase of inlet pressure led to about 100% increase in maximum stress and maximum compressive stress values. Reduction of cap thickness by 50% led to 30% maximum stress value increase and a

nearly 200% increase in maximum compressive stress value. Severe stenosis and 100% eccentricity lead to high flow velocity, high shear stress, negative pressure at the throat, low shear stress and a large re-circulation region distal to the stenosis.

1.1.2 Effect of compliance mismatch on hemodynamics in a stented artery

In what it follows, the focus is placed on understanding of compliance mismatch due to stent implant from the viewpoint of fluid-structure interactions (FSI). One of the early studies focused on flow in a channel with a collapsible segment. Pedley (1992) studied stokes flow in a channel with a collapsible segment. He modeled a compliant wall as a thin elastic membrane and investigated whether the flow-induced variations in the longitudinal wall tension could lead to the breakdown of steady flow. In his iterative numerical approach, it was found that the viscous shear stresses exerted by the fluid at the wall cause the longitudinal tension to decrease as the downstream end of the tube is approached. Luo and Pedley (1995) furthered the study by considering variable wall tensions. They investigated a steady flow in a 2-D channel with one plane rigid wall and with a segment of the other wall replaced by an elastic membrane. They used a standard 2-D Navier-Stokes (N-S) solver for the flow field, and iterated for the wall position. Their studies showed that with an increase of Reynolds number while fixing the membrane tension, the upstream membrane bulges and the downstream membrane constricts. In order to explain self-excited oscillations experimentally found in a finite length of collapsible tube, Luo and Pedley (1996) studied an unsteady flow in a 2-D collapsible channel. They concentrated on the instability of the steady solution and the details of the resulting oscillations when it is unstable, by studying the time-dependent problem. They found that the steady solutions become unstable as tension falls below a certain value and as a consequence, steady flow gives way to self-excited oscillations. Luo and Pedley (1998) furthered their study by considering the effects of wall inertia on unsteady flow in a 2-D collapsible channel. They found that a different type of self-excited oscillation, a form of flutter, is superposed on the original large-amplitude, low-frequency oscillations.

A major alteration in mechanics of a stented artery is an abrupt compliance mismatch at the junction between the stent ends and the host arterial wall. It is believed that this compliance mismatch affects both the vessel hemodynamics and wall mechanics. Various issues related to mechanical behavior of the stented artery have been examined by a number of researchers. Nicoud (2002) assessed the amount of pressure-wave reflexion related to the endovascular stenting of an elastic artery neglecting the details of the stent structures and investigated the changes in the blood motion that can be expected in relation to the compliance mismatch. In his study, the stented section of the vessel is modeled as an elastic duct, whose compliance is less than the non-stented artery. His results showed that the effect of the wall-motion mismatch on the wall shear stress is larger in the medium part of the stented region at systole than in the non-stented artery. At diastole, the cross-sectional area within the stent is larger and the wall shear stress is smaller. In the transition zones between the endovascular prosthesis and the elastic artery, the stresses experiences larger fluctuations, especially at systole. Extra stress is generated in the upstream transition zone, which acts as a convergence. Conversely, the downstream buffer region acts as a divergence at systole and tends to decrease the stress. From the local hemodynamic point of view, the amplitude of the wall shear stress is drastically increased (by 45-50% at the stent level, possibly more in the transition regions) by stenting. This result supports the idea that stenting can induce endothelial dysfunction via hemodynamic perturbations.

It is well known that the elasticity of the vessel wall affects the characteristics of pulsatile flow within a vessel (Alderson and Zamir, 2004). The presence of a rigid segment within an otherwise elastic vessel further complicates this effect because the flow must deal with a stepwise transition from elastic to rigid boundary conditions as it enters the rigid segment and the reverse when it exits. These transition sites represent sites of impedance mismatch and thus sites of wave reflections. Alderson and Zamir (2004) investigated the effects of stent stiffness on local hemodynamics with particular reference to wave reflections. They reported that the presence of the stent within the larger diseased vessel has the effect of producing higher pressure at the vessel entrance than at exit. The basic reason for this is that wave propagation within the stent is abated because of its relative

rigidity. More specifically, wave reflections returning to the vessel entrance produce increased pressure there, while waves transmitted through the stent emerge with lower amplitude because of the abating effect of the stent. A short stent placed near the entrance of the diseased vessel may be favored clinically.

The abrupt change in compliance at the junction of a rigid stent and host artery may be in part responsible for the failure of the stents. Such an abrupt change would create an abnormally large stress concentration at the junction, initiating an adaptive response in the artery wall that would include tissue growth that may lead to restenosis (Mohammad et al.). This aspect has been recognized and studied by Surovtsova (2005), who presented a model of blood flow in compliant vessel consisting of two elastic tubes with different Young's modulus and investigated the mechanical effects caused by the local stiffening of an artery (due to the vascular prosthesis). The high flexure concentration closed to the compliance jump has been observed.

Berry et al. (2002) investigated the hemodynamics and wall mechanical consequences of the compliance matching stent both in vitro and in vivo. Their study helped understand mechanical environment in arteries with stent better. They observed the acute in vivo response of a compliance matching stent (CMS), By using finite element analysis, they assessed the solid mechanical behaviour (compliance and stress) of the compliance matching stent in a stent/artery hybrid structure and compared with a non-compliance-matching (Palmaz stent). Their results showed that although both stents substantially reduced the compliance of the artery, the transition between the host artery and stent was more gradual with CMS. The compliance was reduced in the rigid region by approximately 60% for the CMS and nearly 90% for the Palmaz stent. Also the CMS significantly reduced circumferential stress concentration in the arterial wall when compared to a rigid stent. These results may establish compliance matching criteria for stent design.

However, it should be noted that the studies aforementioned were based either an oversimplified model or a linear model that considers only the global effect of the

compliance mismatch. While the previous work has greatly aided the understanding of the relationship between compliance mismatch and in-stent restenosis, there remain many issues to be further investigated such as the effects of compliance mismatch on blood flow in a nonlinear artery/stent system, the effects of Reynolds number of the flow, and the ratio of elasticity and step size of stent etc. Further understanding of the hemodynamics and wall mechanics of compliance matching stent under different conditions should be useful for identifying the flow pressure, wall shear stress distribution and wall principal stress distribution inside the tube wall. In particular, a better understanding of stent/artery interaction will be helpful for the design of a better stent in the further research.

1.2 Study objectives

In this study, our objective is to investigate the effects of compliance mismatch on blood flow in a nonlinear artery/stent system and to achieve better understanding of influence of the artery/stent geometric parameters and wall elasticity on hemodynamics and wall mechanics of stented vessel. A fully coupled fluid-structure interaction analysis of pulsatile blood flow in a simplified model (an axisymmetric thin tube) is presented here. The simulations employ finite element analysis ADINA and incorporate a nonlinear, isotropic, hyperelastic model for the arterial wall. The Navier-Stokes equations are used as the governing equations for the fluid. ADINA is a finite element analysis system capable of solving problems with fluid-structure interactions. Its capability in solving FSI problems was reviewed in a recent paper (H. Zhang et al., 2003). This study starts with modeling a nonlinear axisymmetric artery/stent tube with a constant cross section as a basis case. Then the radius of the stented segment is slightly changed for comparisons. The physical parameters and geometrical dimensions are not intended to accurately represent physiological values. Here the artery is modeled with a length of 13.2 cm at the proximal segment of stent and 3.2 cm at distal. Lumen diameter of 0.8 cm and thickness of 0.04 cm are chosen in this study. The stent, with a length of 1.6 cm is assumed to have the same diameter and thickness as that of the artery. A modification of this geometry is also studied in which the thickness of the stent is increased to 0.1 cm for the simulations.

Finally the study looks into the fluid dynamics and wall mechanics of a compliance mismatch stent including the pressure field, velocity profile, wall stress and deformation in artery/stent structure with axisymmetric constrictions subject to prescribed inlet pressure and outlet pressure and zero external pressure. In summary, the main objectives in this study is to investigate the effects of elasticity and pressure conditions on the pressure field, flow velocity field, wall stress and deformation, and shear stress along the arterial wall.

Chapter 2 Model and Parameters

2.1 The artery/stent model

A stent is a metal or plastic tube (see Figure 2.1) inserted into an abnormally narrowed or closed conduit (such as an artery or duct) in the body. It serves to keep the conduit open and maintain the blood flow.

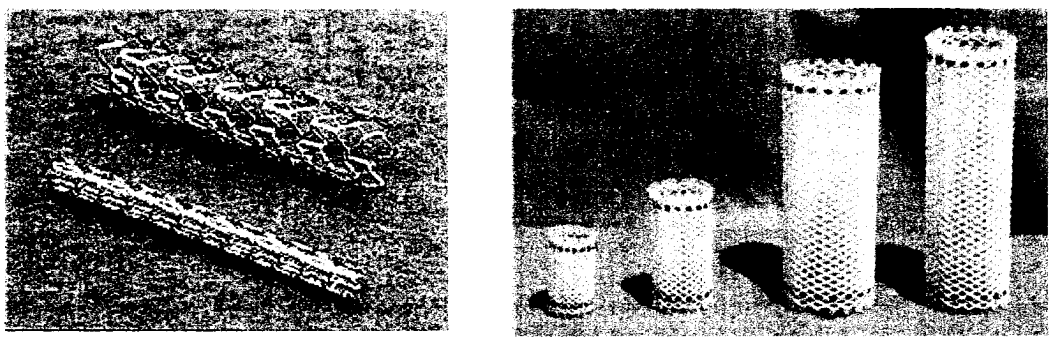

Figure 2.1: Stent[3] designs available in today's market.

In this study, the artery/stent system, shown in Figure 2.2, was assumed to be an axisymmetric thin tube, made of a hyperelastic, isotropic, incompressible and homogeneous material with a density of 1 g/cm^3. The undisturbed artery was chosen to have a diameter , D_0 = 0.8 cm, a wall thickness, h of 0.04 cm, length, Le of 13.2 cm upstream of stent and a length, Lo of 3.2 cm downstream. Le was chosen such that the flow was fully developed at the stent inlet. Two stent wall thicknesses were investigated; hs of 0.04 cm and 0.1 cm (see figure 2.3). For the two cases, the stent had a length, Ls of

[3] www.hc.unicamp.br/.../ lab-cateterismo.shtml,

1.6 cm. The flow was assumed homogenous, incompressible and Newtonian with a density, ρ_f of 1 g/cm^3 and a kinematic viscosity, ν of 0.04 cm^2/s.

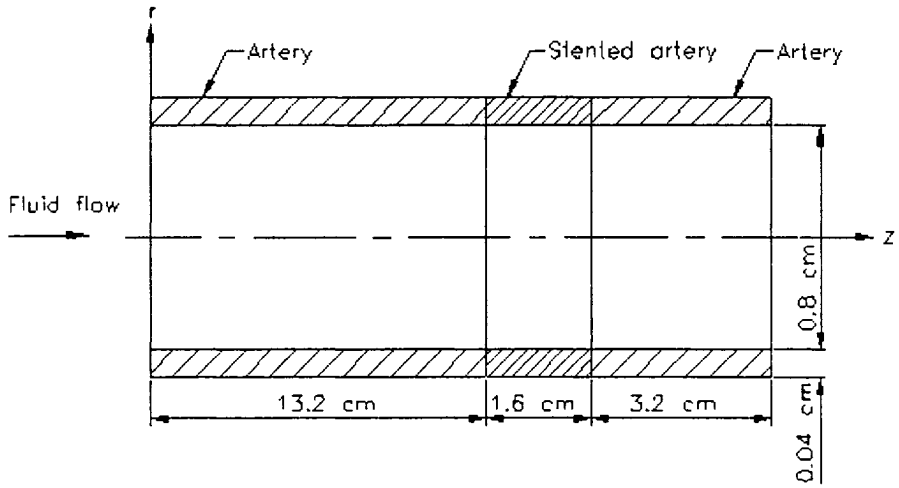

Figure 2.2: Stented artery with a uniform wall thickness

The stent was chosen to have Young modulus, E_s, of $E_s / E_a = 1, E_s / E_a = 5$, $E_s / E_a = 10$ and $E_s / E_a = 100$, where E_a denotes the Young's modulus of the artery (Mooney-Rivlin material).

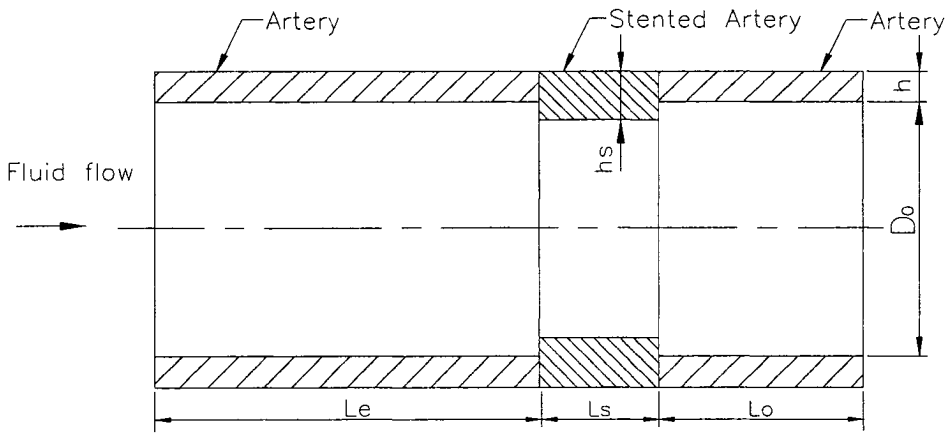

Figure 2.3: Stented artery with a non-uniform wall thickness

2.2 Loading

In this study, the flow was driven by a pulsatile pressure at the artery/stent system inlet given by:

$$p_i = A + B\sin(\omega t + \pi/2) \quad \text{dyn/cm}^2 \tag{2-1}$$

where, $A = 3600$ dyn/cm^2, $B = -900$ dyn/cm^2, $\omega = 2\pi$ is the frequency and t is the time. Although the above pressure time function is different from the actual cardiac cycle, it captures the oscillatory nature of the blood flow in human arteries. At the outlet, however, the pressure was chosen to be time-independent and its constant value was varied to attain the desired Reynolds numbers. The outlet pressure values were selected to be 0, 600, and 1800 dyn/cm^2 which resulted in Reynolds numbers, R_e, based on the diameter of the undisturbed artery, of 1200, 920 and 620 respectively. The Strouhal number, $S_t = \omega D_0 / \bar{U}$ where $\bar{U}$ is the bulk velocity at the artery/stent system inlet, was equal to 0.084, 0.109 and 0.164 corresponding to Reynolds numbers 1200, 920 and 620 respectively. A similar Strouhal number (0.165) has been reported by Shi (1997). The corresponding frequency parameter (Womersly number) $\alpha = D_0 / 2\sqrt{\omega/\upsilon}$ was estimated to be 5.01.

Figure 2.4 shows a velocity profile at the inlet of the test section for the simulation conditions: a zero outlet pressure, the entrance average flow velocity $\bar{U} = 59$ cm/s and a kinematic viscosity, ν = 0.04 cm^2/s. Using the actual diameter $D_0 = 0.79$ cm, the Reynolds number $R_e = D_0\bar{U}/\nu = 1165.3$. Note that $D_0 = 0.8 - 2\times 0.005 = 0.79$ where 0.005 is the wall displacement at the inlet.

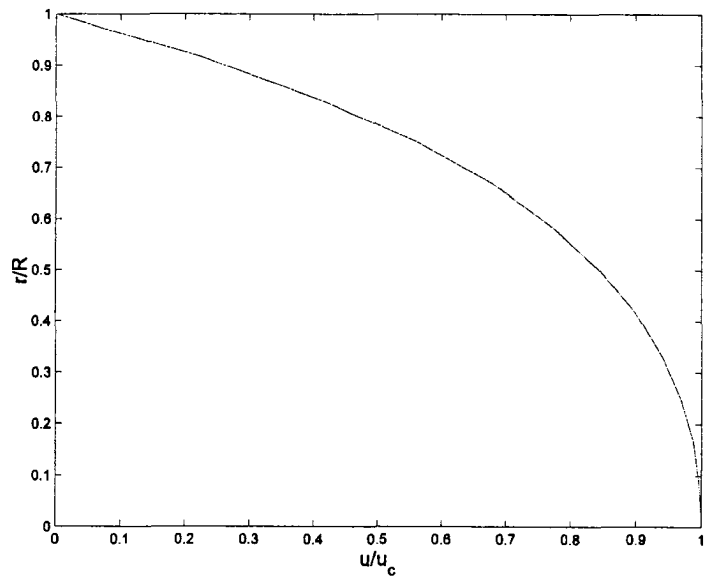

Figure 2.4 Velocity profile at the inlet of the test section for $R_e = 1165.3$, t=0.5 s

Chapter 3 Numerical Approach

The flow in the artery/stent system described in Chapter 2 is a nonlinear fluid-structure interaction problem which is challenging to solve analytically. Therefore, the problem is generally tackled by numerical methods. ADINA is a commercial software that employs finite element analysis (Appendix) and is capable of simulating such a fluid-structure interaction problem. In this Chapter, The equations describing the model as well as the method of solving for the flow and the structure properties will be outlined.

3.1 Governing equations and boundary conditions

3.1.1 The fluid model

The governing equations for the fluid domain are the continuity and Navier-Stokes equations with the assumptions of homogenous, incompressible, and Newtonian flow. An Arbitrary Lagrangian Eulerian (ALE) formulation is used to solve the problem with Fluid-Structural Interaction. In this study, no-slipping boundary condition is assumed between the fluid and the wall. The external pressure is set to zero. The governing field equations can be described by mass and momentum conservation as following:

Continuity:

$$\nabla \cdot \mathbf{u} = 0 \tag{3-1}$$

Momentum:

$$\rho_f \partial \mathbf{u} / \partial t + \rho_f \mathbf{u} \cdot \nabla \mathbf{u} + \nabla p - \mu_f \nabla^2 \mathbf{u} = \rho_f \mathbf{f}_f^B \tag{3-2}$$

Pressure conditions:

$$p\big|_{inlet} = p_1(t) \tag{3-3}$$

$$p\big|_{outlet} = p_2 \tag{3-4}$$

where **u** denotes the fluid velocity vector, ρ_f the fluid density which is chosen as 1 g/cm^3 and μ_f the fluid dynamic viscosity which is assumed to be 0.04 g/cm/s in this study. p_1 and p_2, described in Chapter 2, are the inlet and outlet pressure, respectively. $\mathbf{f}_f^B$ is the body force vector of the fluid medium. In this study this term has been neglected.

3.1.2 The structure model

The governing equation for the structure domain is the momentum conservation equation given by:

$$\rho_s \partial^2 \mathbf{d} / \partial t^2 - \nabla \cdot \sigma^s = \rho_s \mathbf{f}_s^B \tag{3-5}$$

where **d** denotes the displacement vector of the structure, ρ_s the mass density of the structure. $\mathbf{f}_s^B$ is the body force vector per unit volume. σ^s is the structure stress tensor. The Cauchy-Green deformation tensor σ_{ij}^s can be determined by:

$$\sigma_{ij}^s = \lambda \varepsilon_{kk} \delta_{ij} + 2\mu \varepsilon_{ij} \tag{3-6}$$

where λ and μ are the Lame constants of the media. δ_{ij} is the Kronecker delta, and ε_{ij} are the Green-Lagrange strains defined as:

$$\varepsilon = \frac{1}{2} \frac{l^2 - l_0^2}{l_0^2} \tag{3-7}$$

where l and l_0 are the current length and original length.

Assuming that $\mathbf{f}_s^B$ is zero and ρ_s is negligible, the equilibrium equations and the boundary conditions used to determine the displacement (deformation) of the artery wall are given by (Tang et al., 1999)

$$\sigma_{ij,j}^s = 0, \tag{3-8}$$

$$\mathbf{d}^s|_{innerwall} = \mathbf{d}^f|_{innerwall}$$

$$\sigma_{ij}^s \cdot n_j|_{outerwall} = 0, \tag{3-9}$$

$$\sigma_{ij}^s|_{innerwall} = \sigma_{ij}^f|_{innerwall}, \tag{3-10}$$

where $\mathbf{d}^s$, $\mathbf{d}^f$ are the displacement vectors for the structure and the fluid, respectively, σ_{ij}^s and σ_{ij}^f are the Cauchy stress tensors for the structure and the fluid, respectively, and $.,j$ stands for the derivative with respect to the j th variable.

The relation between the strain-energy density function and the stress-strain relation is given by the following formula:

$$\sigma_{ij} = p_{ij} + \frac{\partial W}{\partial \varepsilon_{ij}} \tag{3-11}$$

where W is the strain-energy density function and p_{ij} the local hydrostatic pressure. ε_{ij} the Green-Lagrange strains. The strain-energy density functions can be made very material specific and is therefore often used to characterize biological tissues. The Mooney-Rivlin material model is based on the following expression (ADINA R & D, Inc., 2004) which can adequately describe the non-linear stress-strain relationship of elastic arterial tissue:

$$W = c_1(I_1 - 3) + c_2(I_2 - 3) + c_3(I_1 - 3)^2 + c_4(I_1 - 3)(I_2 - 3) + c_5(I_2 - 3)^2 + c_6(I_1 - 3)^3 + c_7(I_1 - 3)^2(I_2 - 3) + c_8(I_1 - 3)(I_2 - 3)^2 + c_9(I_2 - 3)^3 + D_1[e^{D_2(I_1-3)} - 1] \quad (3\text{-}12)$$

where:

$$I_1 = \lambda^2 + 2/\lambda, \quad I_2 = \lambda^{-2} + 2\lambda \quad (3\text{-}13)$$

c_1 to c_9 and D_1 to D_2 are material constants. I_1 and I_2 are the invariants of the deformation tensor (Bathe, 1996), λ is the axial stretch ratio. In this study, an initial axial stretch of 3.4% was imposed on the entire artery. The arterial material was modeled by the standard two-term Mooney-Rivlin material law (ADINA R&D, INC., 2004), given by:

$$W = c_1(I_1 - 3) + c_2(I_2 - 3) + D_1[e^{D_2(I_1-3)} - 1] \quad (3\text{-}14)$$

with c_1 = 46 000 dyn/cm^2, c_2 = 0, D_1 = 36 000 dyn/cm^2 and D_2 = 2.0 suggested by Tang et al. (2004) were chosen for the arterial wall. The arterial wall, E_a, is written as:

$$E_a = 6[(c_1 + c_2) + D_1 D_2] \quad (3.15)$$

and the Young's modulus for the stented part of the artery was changed by adjusting the constants in equation 3.15.

As pointed out in Section 1.2, the chosen physical parameters and geometrical dimensions are not intended to accurately represent the physiological values of the actual stented artery. However, these parameter values were chosen following the common practice used in the literature. For example, the Reynolds numbers used in the study are

620, 920, 1200. The Reynolds number of the blood in artery is known to be around 500[4]. The artery material is chosen to be the Mooney-Rivlin one which has been used in various studies, for example Tang et al. (2004).

3.2 The fluid-structure interactions simulations

3.2.1 The ADINA software

The fully coupled fluid-structure models are solved by ADINA which uses a finite element approach to solve the equations of fluid dynamics and the finite element formulation for the structural dynamics.

The main idea of the solution method used in this study can be described as follows: Starting from an initial domain, the Navier-stokes equations are solved. Then the equilibrium equations, Eq.(3-8), are solved with input from the flow field to determine the wall displacement. Then the Navier-stokes equations are solved again over the newly adjusted domain. This process is repeated until desired accuracy is reached. It is known that convergence is hard to achieve when the wall is significantly compliant. ADINA uses an automatic incremental iterative technique to reach convergence when the regular iterative procedure fails. At a given iteration step, when convergence from the fluid part is reached, ADINA takes the changes of the pressure and stress fields of the fluid as input and tries to determine the corresponding changes of the wall displacement. If convergence for the wall part cannot be obtained, ADINA reduces the size of the input by haft and tries to determine the wall displacement in two increments. This is repeated until convergence or a default reduction limit is reached.

[4] www.coheadquarters.com/PennLibr/MyPhysiology/lect5/index.html

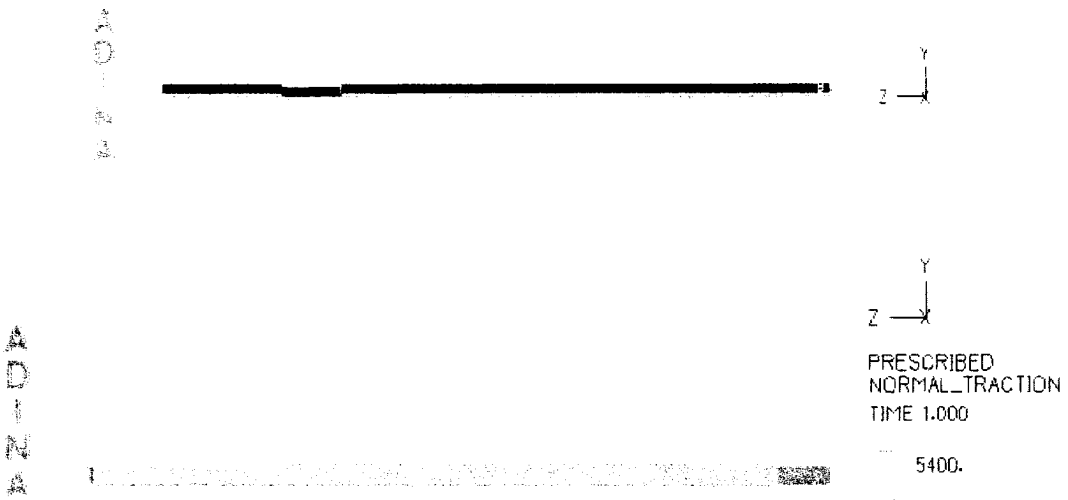

Figure 3.1. The wall and fluid domain

3.2.2. Solution method

The solution is assumed to be axisymmetric with respect to the yz-plane (Fig. 3.1), so only haft of the whole domain is needed for the volumes. For the wall model, the tube is divided into three parts corresponding to the entry, stented, and outlet part. The $v \times u$ mesh used for subdivisions is $1 \times (264+80+64)$ with finer mesh used for the stented arterial wall in order to obtain an accurate solution. The element types used are 2-D solid, axisymmetric. 4 nodes per element are used. In the ADINA-F model, the fluid domain is also divided into three parts. The mesh used is $12 \times (264+80+64)$. Higher element density is used at the stented part in order to capture the steep velocity gradient there. Recirculation may present there. The element types used are 2-D fluid axisymmetric, 3 nodes triangular elements. The inlet and outlet pressures are imposed using the 'normal traction' option. The inner wall and its corresponding fluid part are defined as the fluid-structure interface (dark line in Figure 3.1). For the fluid model, it is assumed that no-slip

takes place between the fluid and the arterial wall and no penetration of the fluid through the wall occurs.

The mesh densities described above, were chosen based on the best trade-off of computational time and accuracy. The choice was determined by comparing some of the results, to be shown in later Chapters, obtained with the mesh densities used in the thesis (model A) and the same results obtained for a model (model B) whose mesh densities were double that of model A. The data shown in figures 3.2 to 3.4 suggested that both the models gave comparable values. Thus, the mesh densities used for model A were acceptable and thus used throughout the thesis.

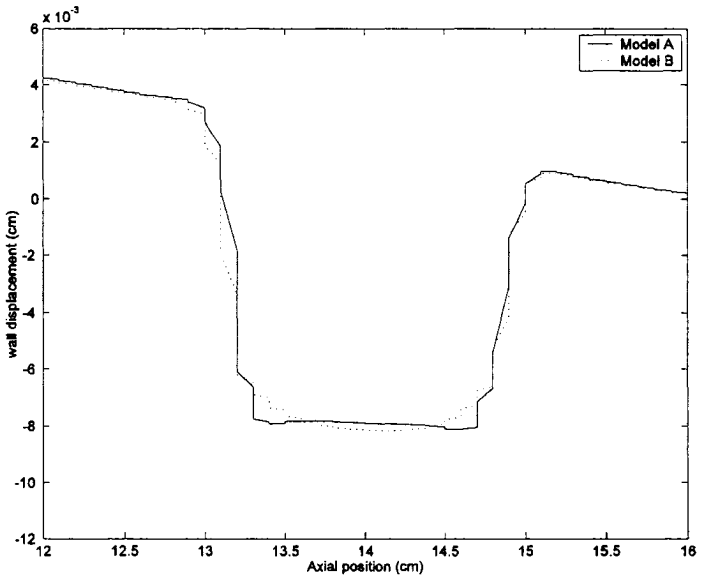

Figure 3.2. Wall displacement for $E_s / E_a = 5$, $R_e = 620$, h_s=0.04 cm, $t = 0.5$ s.

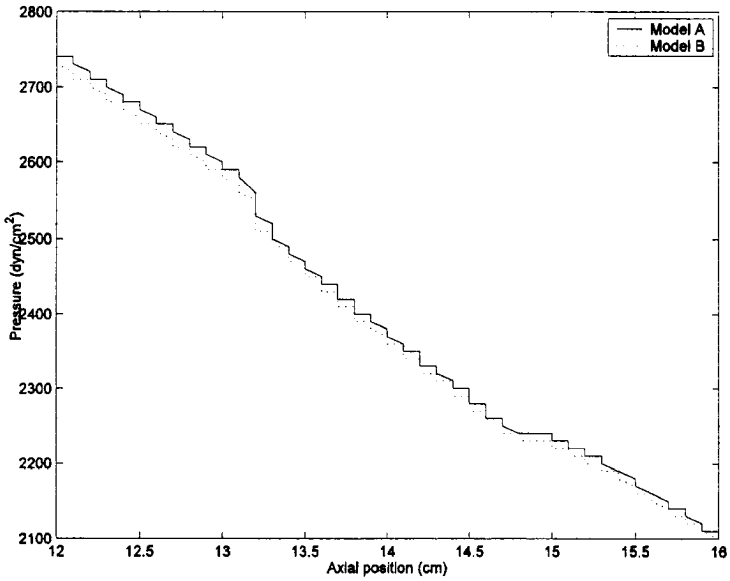

Figure 3.3. Pressure distribution for $E_s / E_a = 5$, $R_e = 620$, h_s=0.04 cm, t = 0.5 s.

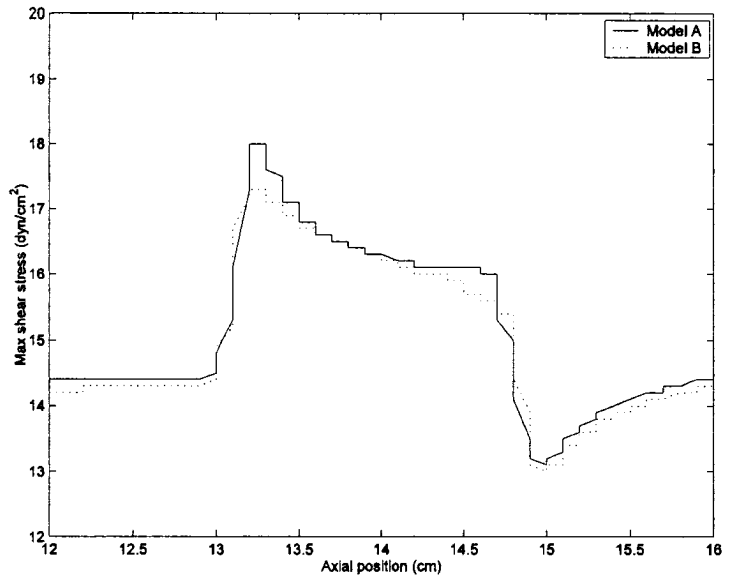

Figure 3.4. Fluid shear stress for $E_s / E_a = 5$, $R_e = 620$, h_s=0.04 cm, t = 0.5 s.

The governing finite element equations for both the solid and fluid are solved by Newton-Raphson iteration (Tang et al., 2004). Convergence is achieved if

$$\left\| f^i - f^{i-1} \right\| / \left\| f^i \right\| \leq TOL \tag{3-16}$$

where f stands for the variables being solved (flow velocity, pressure and wall displacement), i is iteration index, TOL is a specified tolerance. In this study, TOL was selected to be 0.0005 (Tang et al., 2004).

A common way to deal with boundary conditions is no axial motion of the inlet and outlet of the wall (Tang et al., 2004) so that the entire tube would not be dragged away by the flow. To see the effect of such a treatment, we first built a model whose two ends were fixed axially, not radially. To simplify the model, $E_s / E_a = 1$ was assumed and used $R_e = 1200$ which corresponds to $p_2 = 0$. Figure 3.2 shows the wall displacements at four different moments. At $t = 0.25$ s (solid line), the right portion of the wall moves up while the left portion of the wall moves down. In the meantime, the wall is deformed such that the wall is curved. When the pressure reached its maximum at $t = 0.5$ s (dotted line), the wall's upward motion reached its maximum as well. When the pressure fell ($t = 0.75$ s) (dash dot line), the wall moved downward. These results indicate a need to restrict the wall's ends in the radial direction. Thus in the following models, the two ends of the wall are fixed both axially and radially. Figure 3.5 also gives a reference for the wall deformation without compliance mismatch.

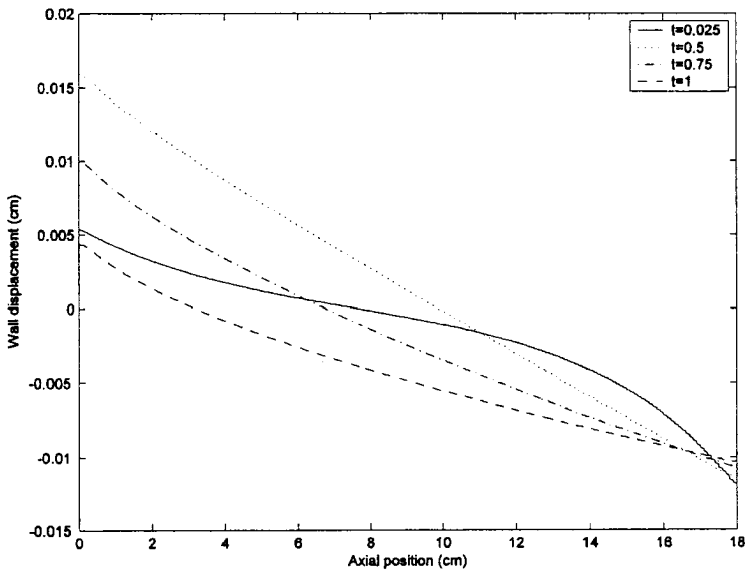

Figure 3.5 Wall displacement at different time for $E_s / E_a = 1$, $R_e = 1200$

Chapter 4 Simulations Results

The objective of the present work is to investigate the effects of the stent geometry, its compliance and Reynolds number on the flow dynamics and wall mechanics of a stented artery when subjected to an inlet pulsatile pressure. For this purpose, two stent geometries were investigated; a stent that had the same wall thickness, hs, as the artery, a stent with a wall thickness of h_s = 0.1 cm. To study the effects of the stent elasticity, the simulations were carried out, for all stent geometries, for values of the modulus of elasticity of the stent, E_s, corresponding to $E_s = E_a$; 5 E_a; 10 E_a and 100 E_a, where E_a is the elasticity of the artery, and at Re = 620. As for the effects of Reynolds number, the simulations were done for the stent geometries mentioned above, at a fixed stent modulus of elasticity $E_s = 5\ E_a$ and for Re of 1200, 920 and 620. The focus will be on the model responses in terms of the wall displacement, wall stress, flow velocity field, and pressure distribution. The attention will be on the region between $z = 13.2$ cm and $z = 14.8$ cm which includes the proximal region, stent region, and the distal region of the compliance mismatch zone. Unless stated otherwise, the results presented here at the moment t = 0.5 s, corresponding to the maximum inlet pressure value.

4.1 Case one: Stented artery with a uniform wall thickness

4.1.1 Elasticity ratio effects

Time evolutions of the wall displacement, relative to the undisturbed tube, at the proximal and the distal points for cases $R_e = 620$, $E_s / E_a = 1$, 5, 10 and 100 are shown in Figure 4.1 (a) and (b). It can be seen that the case of $E_s/E_a > 1$ resulted in radius reduction at the both the proximal and distal points with amplitudes being larger at the proximal point than at the distal point. Also, the wall displacements followed the pressure time

variations at the inlet and the amplitude decreased as the stent stiffness increased, and for the largest elasticity ratio studied here (E_s/E_a = 100) the wall displacement became roughly independent of time.

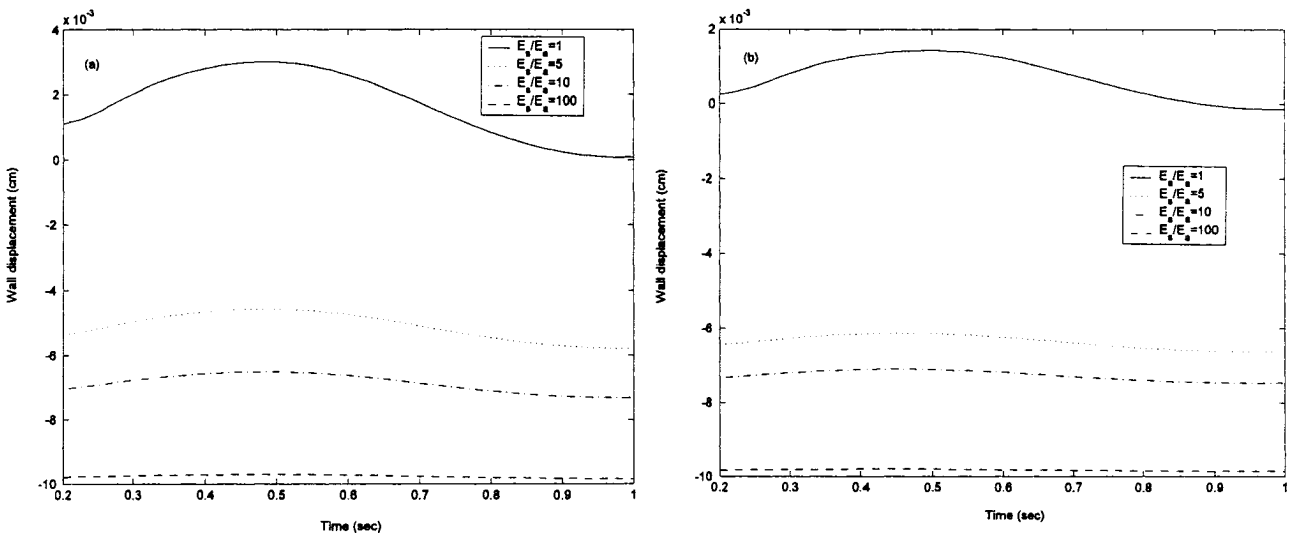

Figure 4.1 Time evolutions of the wall displacement at the proximal point (a) and distal point (b) of the stent for $R_e = 620$

Figure 4.2 shows the wall displacement at t = 0.5 s, relative to the undisturbed tube, for different elasticity ratios and at $R_e = 620$. When E_s/E_a = 1, the wall profile is smoothly varying, generally as response to downstream variation of the wall pressure (see figure 4.3). As the elasticity ratio is increased, the wall deformation varied continuously in the proximal and distal regions but drastic wall shape changes occurred around the compliance transition zones, consistent with Berry et al. (2002) who assumed linear elastic and an isotropic material property for the arterial wall. Considering E_s/E_a = 1 as a reference where the properties are indicated by the subscript *rf*, estimates of radius reductions, $\Delta R/R_{rf}$, at the stent inlet were estimated to be 2.5% and 3.3% for E_s/E_a = 5 and E_s/E_a = 100 respectively.

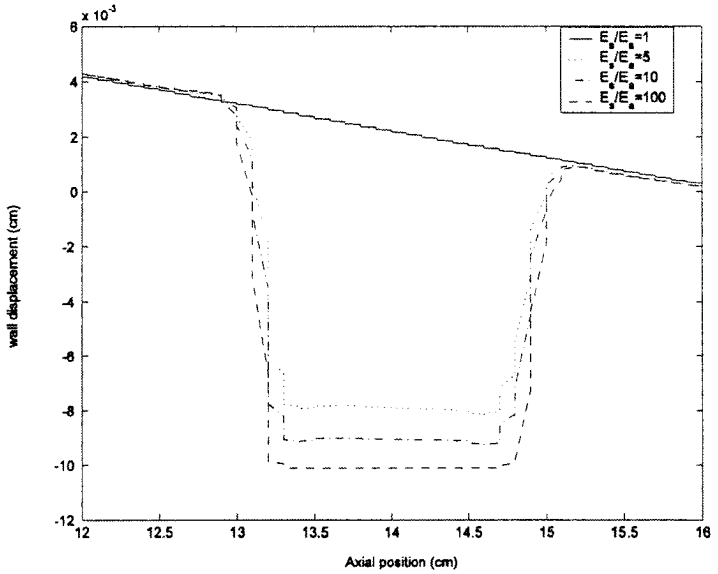

Figure 4.2: Wall displacement for $R_e = 620$

Figure 4.3 displays plots of the axial wall pressure variations at t = 0.5 s. The pressure decreased monotonically in the proximal and distal regions of the artery/stent system but for $E_s/E_a > 1$, the pressure in the stent slightly decreased as a response to the area reduction in those regions. This change apparently induced wave reflections which resulted in a slight increase in the pressure upstream of the stent in agreement with Alderson and Zamir (2004). The pressure drop across the stent inlet, $\Delta P/P_{rf}$, were estimated to be 1.2% and 1.6% for E_s/E_a = 5 and E_s/E_a = 100 respectively. Compared with the case $E_s / E_a = 1$, for each individual one, the pressure gradient develops at the proximal junction of the stent and recovers at the distal end. This is due to wall shape changes more at those places as the wall stiffness increases. This phenomenon is generally in agreement with what was reported in the study conducted by Tortoriello and Pedrizzetti (2004).

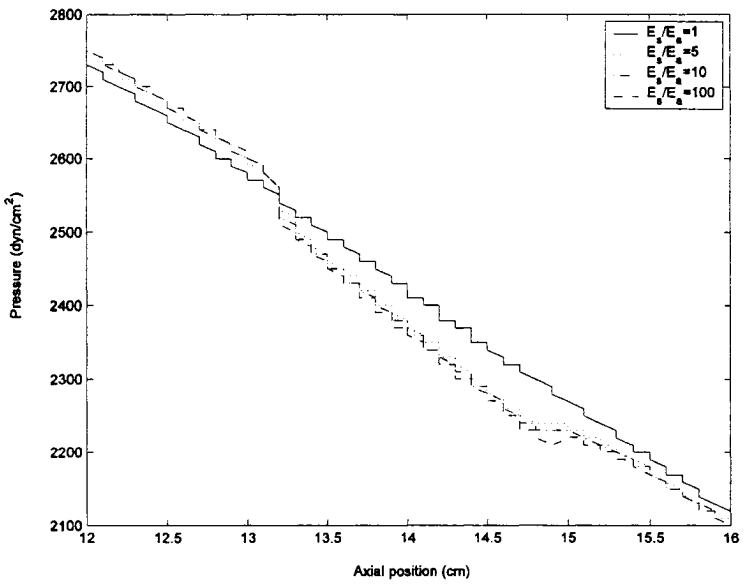

Figure 4.3: Pressure distribution along the wall for $R_e = 620$.

Time evolutions of the wall radial and axial velocities at the proximal and the distal points of the stent are shown in Figure 4.4 (a and b) and Figure 4.5 (a and b). These display the expected behavior with a minimum corresponding to the maximum pressure (or wall displacement). The wall radial velocity shown in Figure 4.4 (a) demonstrates that the wall deformation follows the pulsating pressure variation. In other words, the pulsating pressure causes a deformation wave traveling through the artery wall. This result agrees qualitatively with those present in G.Pontrelli (2001).

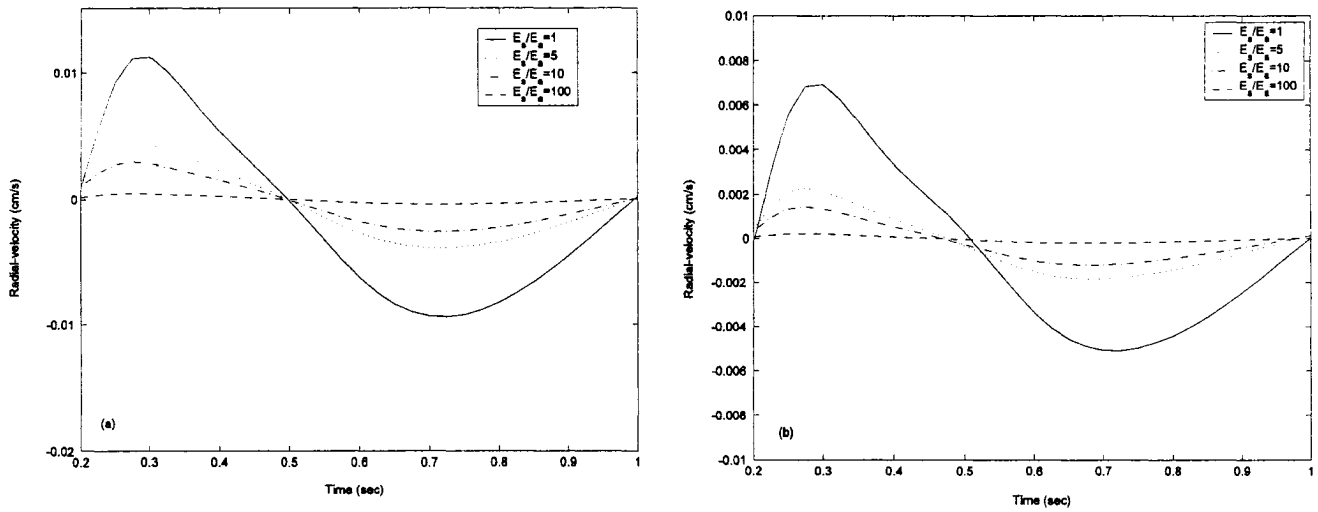

Figure 4.4 Time evolutions of the wall radial velocities at the proximal point (a) and distal point (b) of the stent for $R_e = 620$

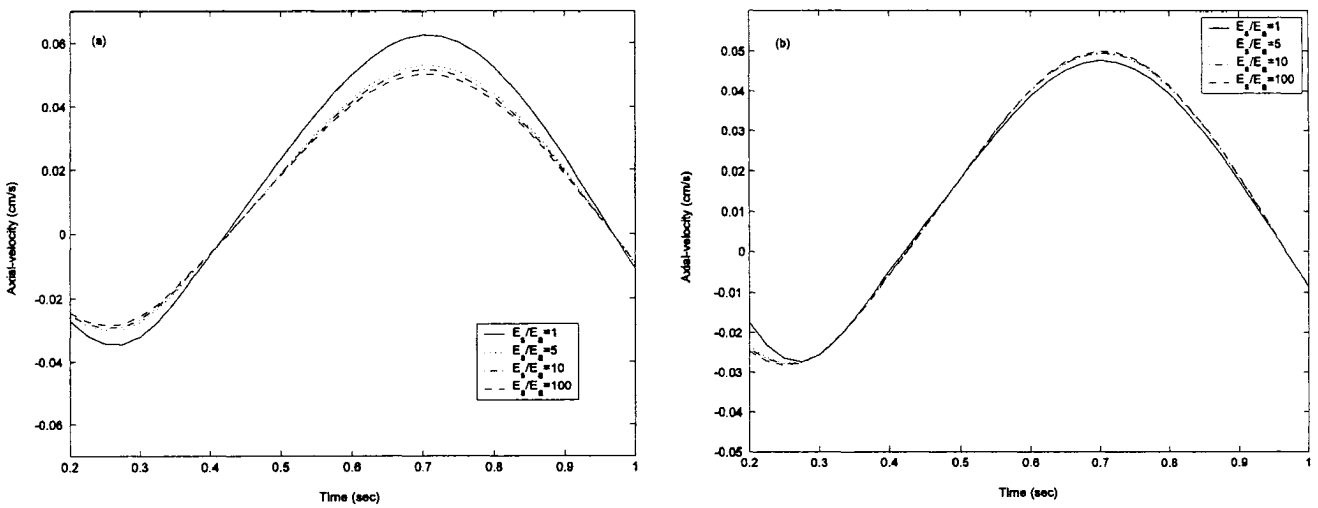

Figure 4.5 Time evolutions of the wall axial velocities at the proximal point (a) and distal point (b) of the stent for $R_e = 620$

Figure 4.6 (a) and (b) shows the time evolution of the wall shear stress (solid) at the proximal point (a) and distal point (b) of the stent for $E_s / E_a = 1$, 5, 10 and 100, $R_e = 620$ case. It displayed a time dependence that is remnant of the inlet pressure time function. As opposed to the arterial wall displacement shown in Figure 4.1, the wall shear stress

time evolution retained its form, regardless of the value of E_s/E_a, with a maximum amplitude occurring roughly at $t = 0.5$.

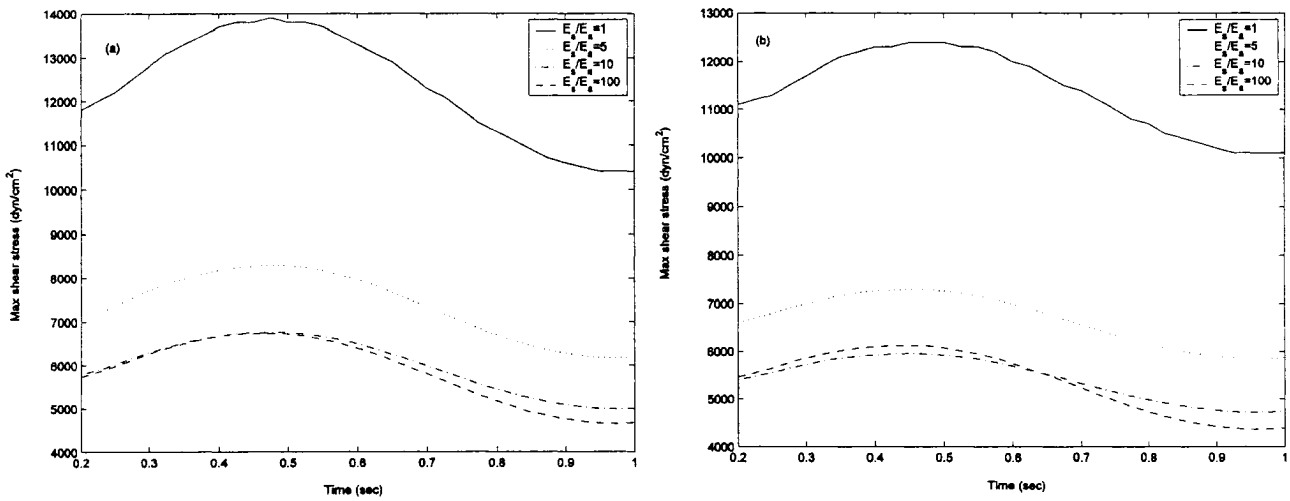

Figure 4.6: Time evolutions of the wall shear stress at the proximal point (a) and distal point (b) of the stent for $R_e = 620$

The increased elasticity ratio seemed to have the largest effect on the fluid shear stress, τ_w, as shown in Figures 4.7 (a) and on the artery wall principal stress τ_p, as shown in Figures 4.7 (b). In Figure 4.7 (a), the fluid shear stress at the wall just ahead of the stent, decreased sharply as the elasticity ratio, E_s/E_a increased from 1 to 5 and remained roughly unaffected as E_s/E_a was further increased.

The wall principal stresses were marked by a sharp increase right at the compliance transition zone as shown in Figure 4.7 (b) in agreement with Nicoud (2002) and Berry et al. (2002). Estimates of the increase in the wall principal stress, $\Delta\sigma_p / \sigma_{p,rf}$, showed that σ_p increased by 64% and 164% for E_s/E_a = 5 and 100 respectively suggesting that the wall principal stress strength at the joints strongly depended on the elasticity ratio. The wall principal stress within the stent, excluding the transition zones, was markedly lower and smoothly varying downstream with no apparent dependence on the E_s/E_a. The fluid shear stress on the other hand, was marked by a sharp increase at the stent inlet but sharply decreased at the stent outlet as displayed in Figure 4.7 (a). This is explained by

the fact that at the wall, the fluid shear stress, τ_w is strongly affected by the pressure gradient, dP/dz. It was observed that this gradient was negative (favourable) at the stent inlet and positive (adverse) at the stent outlet as seen in figure 4.3 resulting in the wall fluid shear stress in Figure 4.7 (a). It is also observed that the increased elasticity does engender appreciable changes the values of τ_w. In fact, estimates of $\Delta\tau_w/\tau_{w,rf}$, were found to be 18.2% and 32.2% for $E_s/E_a = 5$ and 100 respectively.

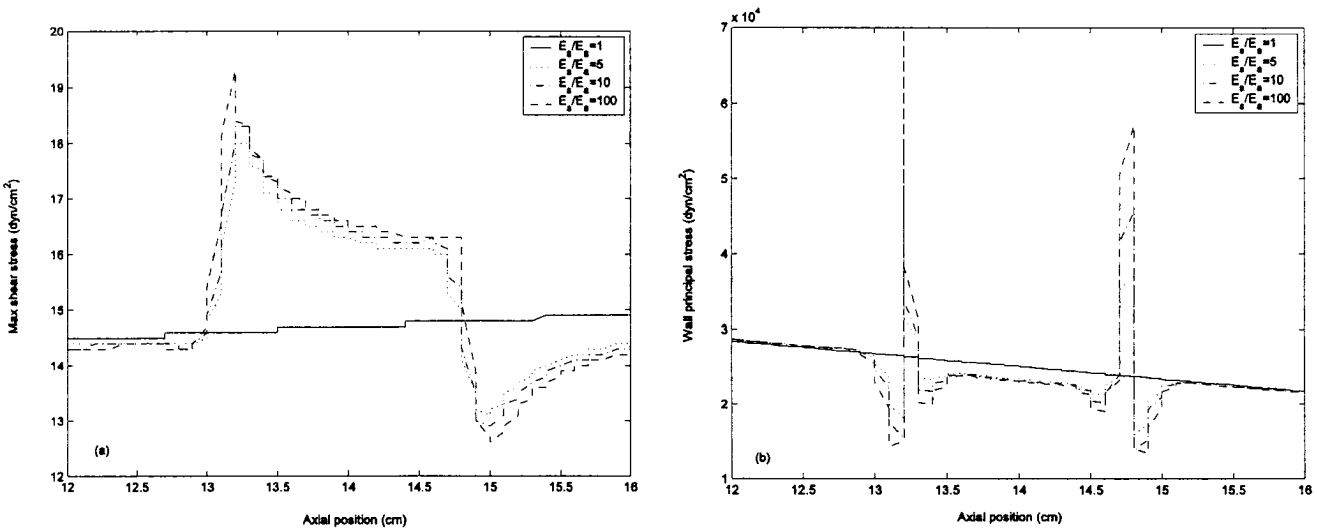

Figure 4.7: (a) Fluid shear stress (b) Wall principal stress for $R_e = 620$.

The estimated values of $\Delta R/R_{rf}$ and $\Delta P/P_{rf}$, suggest that the increased elasticity ratio has only minor effects on the wall shape and on the pressure axial variations and thus on the flow behaviour in the proximity of the stent. In fact, streamline plots for E_s/E_a = 5 and E_s/E_a = 100, at the proximal and distal region of the compliance mismatch zone shown in Figure 4.8 remained roughly unaffected as the elasticity ratio changed from 5 to 100.

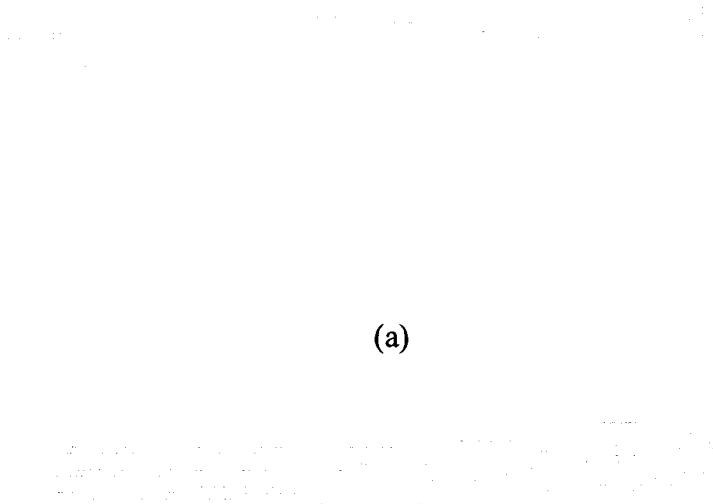

(a)

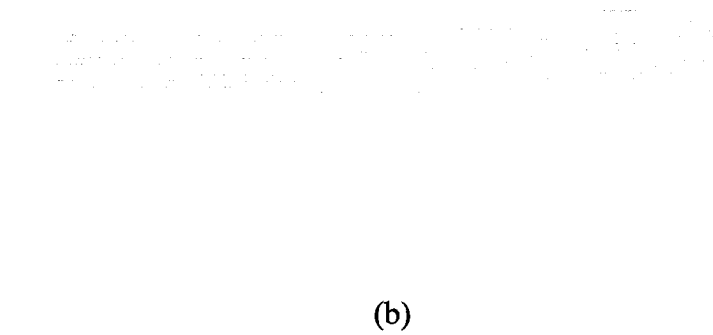

(b)

Figure 4.8: Flow streamlines at t=0.5 s, hs=0.04 cm (a) for E_s/E_a = 5, (b) for E_s/E_a = 100

4.1.2 Reynolds number effects

It was shown in the previous section that the onset of an elasticity ratio, E_s/E_a larger than one, resulted in alteration of the artery/stent wall shape but increasing E_s/E_a beyond five, within the elasticity ratios investigated here, did not result in appreciable further deformations. For this reason, to determine the effects of Reynolds number, *Re*, on the flow dynamics and wall mechanics, the simulations were carried out for *Re* of 1200, 920 and 620 with the elasticity ratio set at $E_s / E_a = 5$ in each case.

Time evolutions of the wall displacement at the proximal point and the distal point of the stented artery for cases of $E_s / E_a = 5$, $R_e = 1200, 920, 620$ are shown in Figure 4.9 (a) and (b). It can be seen that for all Re_e investigated here, the wall displacements at the inlet

and outlet of the stent had time changes similar in form to that of the pressure at the artery/stent inlet, with displacements that are larger at the proximal point than at the distal point.

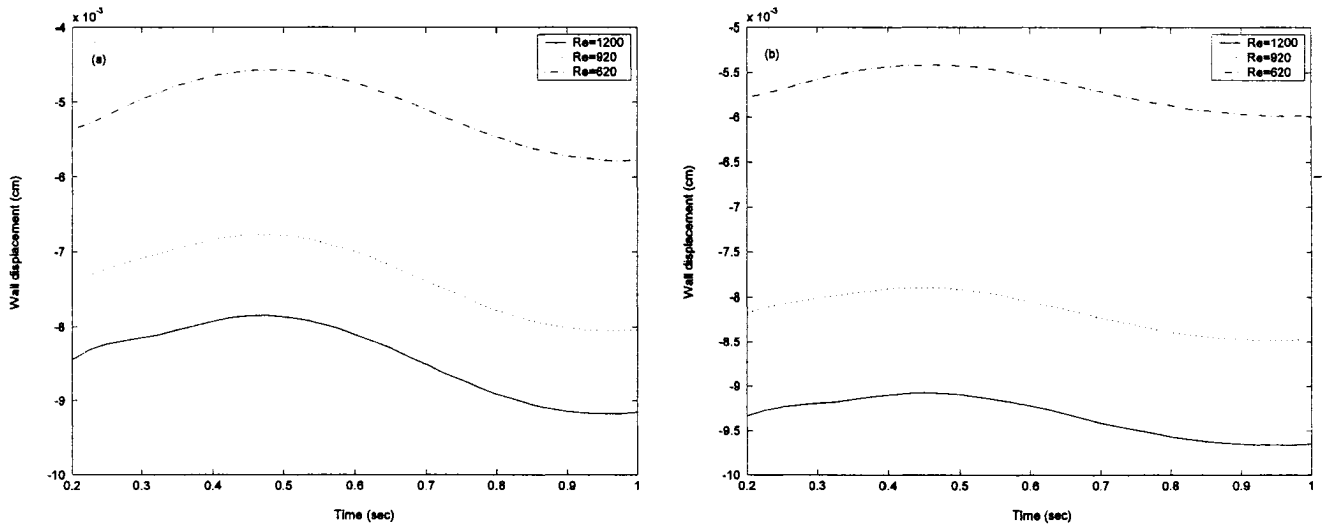

Figure 4.9: Time evolutions of the wall displacement at the proximal point (a) and distal point (b) for $E_s / E_a = 5$

The wall displacements, relative to the undisturbed tube, at t = 0.5 s are shown in Figure 4.10 (a). As expected, the increase in Reynolds number resulted in a smaller radius reduction at the stent inlet because a higher Reynolds number corresponds to a lower outlet pressure such that the overall pressure in the artery/stent system is lower as shown in Figure 4.10 (b). Evaluations of radius reductions at the stent inlet, $\Delta R/R_{rf}$, gave 2.7% and 1.2% for *Re* of 620 and 1200 respectively.

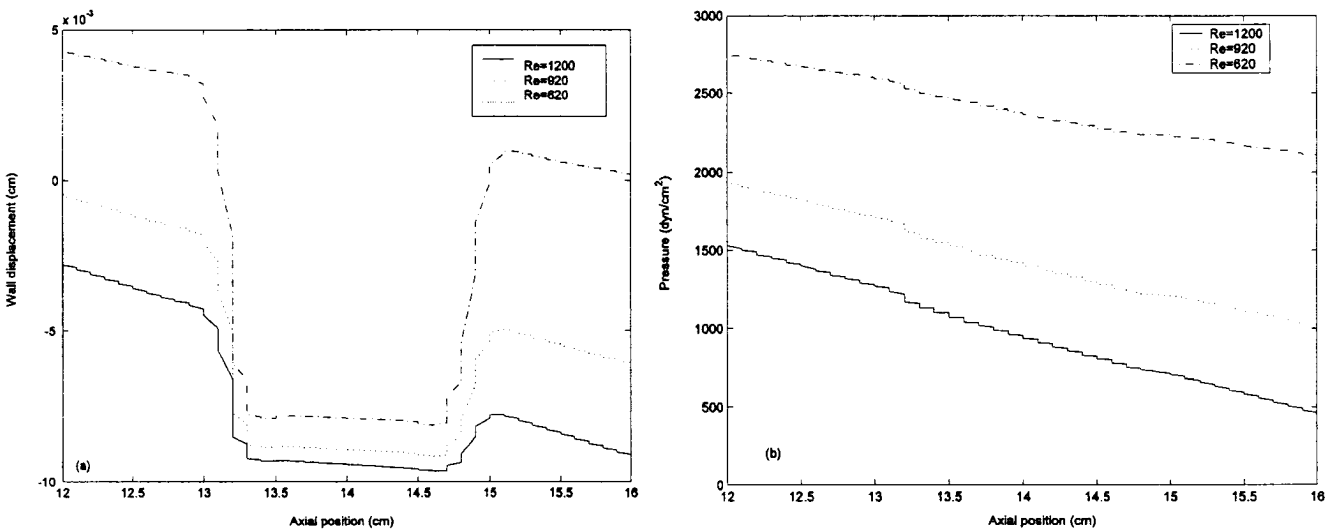

Figure 4.10: Effect of Reynolds number for $E_s / E_a = 5$ on (a) wall displacements; (b) pressure variations.

The wall fluid shear stresses and wall principal stresses for $R_e = 1200, 920, 620$ and $E_s / E_a = 5$ are given in Figure 4.11. The values of Reynolds number was increased by adjusting the pressure at the artery outlet. As expected, the fluid shear stress at the wall increased throughout the artery/stent system with increased R_e. Its behaviour at the junctions as well as in the stented regions remained unaffected as R_e increased. Evaluations of $\Delta\tau_w/\tau_{w,rf}$ at the stent inlet gave 24% and 12% for Re of 620 and 1200 respectively. However, the wall principal stress displayed an opposing trend in that, as R_e increased σ_p decreased. This is due to the fact that the higher Reynolds number is, the lower the overall pressure in the artery/stent system which in turn results in a reduced wall principal stress. Evaluations of $\Delta\sigma_p / \sigma_{p,rf}$ at the stent inlet gave -129% and -150% for Re_e = 620 and 1200 respectively.

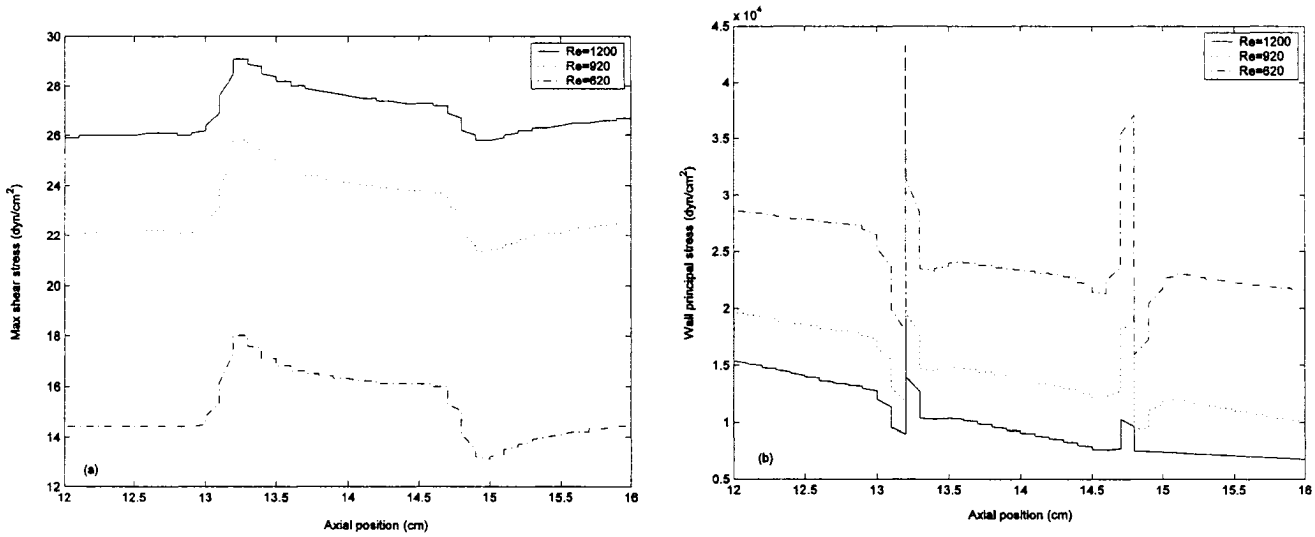

Figure 4.11: (a) fluid wall shear stress (b) wall principal stress for $E_s / E_a = 5$

4.2 Case two: Stented artery with a non-uniform wall thickness

4.2.1 Elasticity ratio effects

The flow simulations were repeated with the same parameters as described in Section 4.1 with the exception that the stent had a thickness of hs = 0.1 cm. This resulted in a radius reduction at the stent inlet, $\Delta R/R_0$, in the undisturbed artery of 15%. Time evolutions of the wall displacement at the proximal point of the stent for $R_e = 620$, $E_s / E_a = 1$, 5, 10 and 100, and hs = 0.1 cm are shown in Figure 4.12 (a). It can be seen that the time variations of the wall displacement roughly followed that of the inlet pressure with maximum amplitude occurring at t of about 0.5 s which decreased with increasing E_s/E_a. As opposed to the case when hs = 0.04 cm, the wall remained a strong function of time even for the largest E_s/E_a. The axial arterial wall shapes at t = 0.5 s are shown in Figure 4.12 (b). The radius reduction at the stent inlet for E_s/E_a = 1 was evaluated to be $\Delta R/R_{rf}$ = 16% suggesting that, even in the case of E_s/E_a = 1, the stent penetrated further into the flow. As E_s/E_a increased to 5, the radius reduction was evaluated to be about 17% and remained nearly unaffected as E_s/E_a increased to 100.

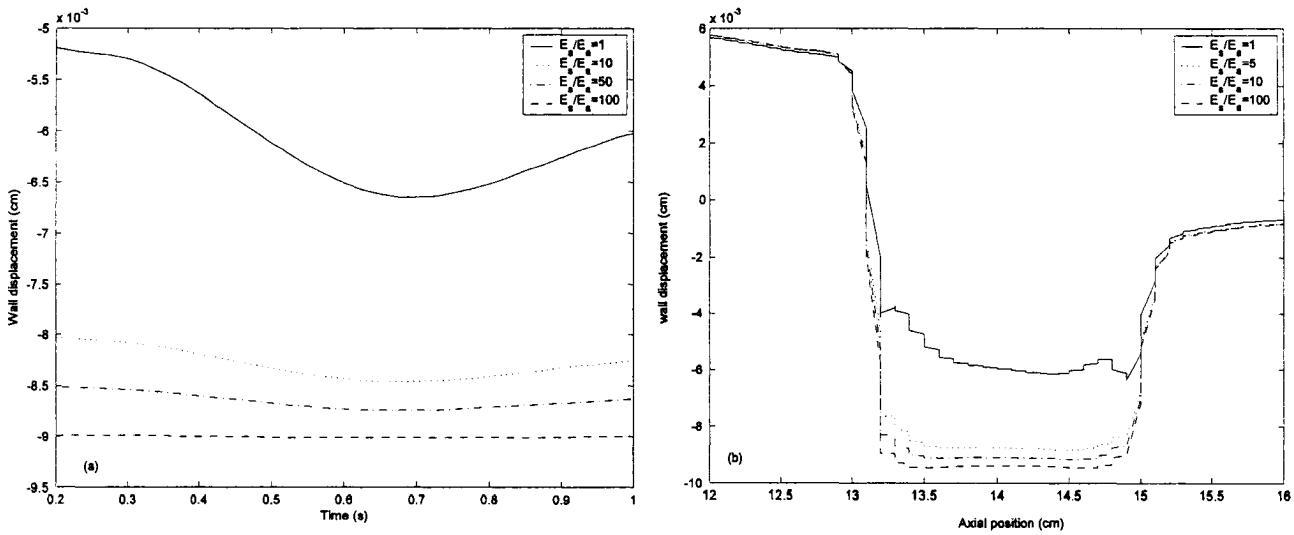

Figure 4.12: (a) Time evolution of the wall displacement (b) Wall displacement for $R_e = 620$ at t= 0.5 s, hs = 0.1cm.

Figure 4.13 (a) is a plot of the wall pressure variations at $t = 0.5$ s. Due to the presence of a step at the stent inlet, the pressure dropped abruptly in the stented region of the artery. The flow adjusted to the low pressure in the stent through a recirculation region as shown in Figure 4.13 (b). It is worth noting that the pressure value at the stent outlet is lower than the pressure at the artery/stent system outlet, p_2, thus the distal flow pressure recovered through a recirculation region as shown in Figure 4.13 (b). The pressure drop, $\Delta P/P_{rf}$, at the stent inlet was estimated to be nearly 32% for all E_s/E_a investigated here. This fact suggested that the flow pressure was, generally, affected by the stent geometry but weakly dependent on the elasticity ratio.

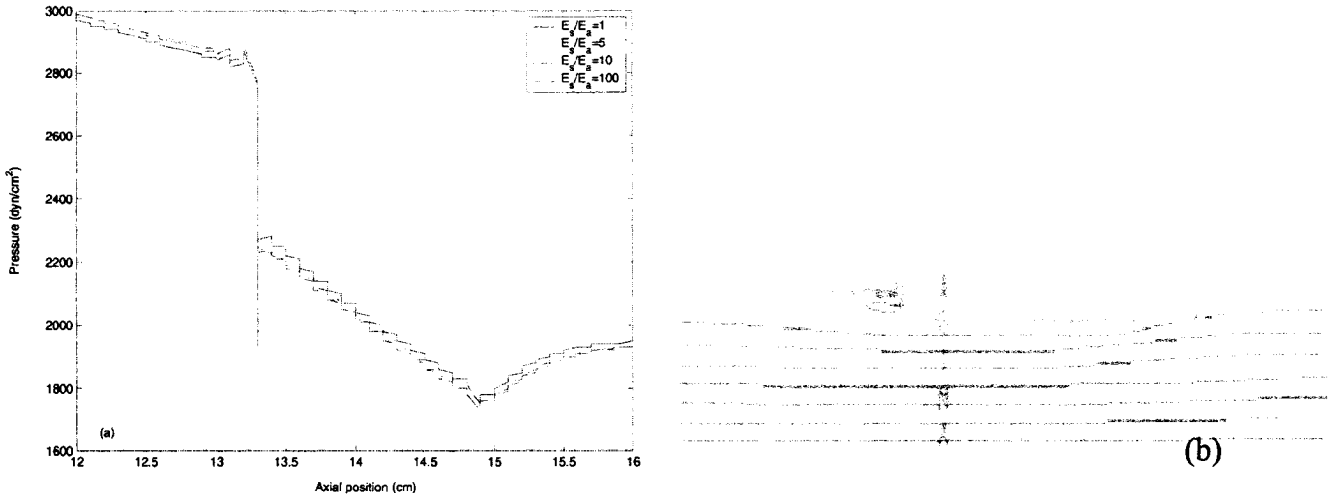

Figure 4.13: (a) Pressure variations (b) Flow streamlines at t = 0.5 s, hs = 0.1 cm.

The wall fluid shear stress and wall principal stress distributions when hs = 0.1 cm, for $E_s / E_a = 1$, 5, 10, 100 at time 0.5 s, $R_e = 620$ are presented in Figure 4.14 (a) and 4.14 (b) respectively. The fluid shear stress generally exhibited an axial variation that resembled the case of hs = 0.04 cm except that it displayed mach larger peak values at the stent inlet and outlet also, it dropped to zero values just ahead and downstream of the stent due to the presence of the separated flow at those regions. The wall shear stress change at the stent inlet, $\Delta\tau_w/\tau_{w,rf}$ was estimated to be 260% irrespective of the elasticity ratio. However, the wall principal stress exhibited a behaviour that is quite distinct from case of hs = 0.04 cm as shown in Figure 4.14 (b). The simulations suggested that, for the values of E_s/E_a investigated here, the wall principal stress decreased abruptly at the artery/stent joints and, for each E_s/E_a, it retained roughly the same value throughout the stent without discontinuous jumps at the compliance mismatch regions. It is also observed that when E_s/E_a > 5, the wall principal stress is compressive (negative) and decreased as E_s/E_a increased. Estimates of the changes in the wall principal stress values at the proximal compliance mismatch zone, $\Delta\sigma_p / \sigma_{p,rf}$ showed that σ_p decreased by roughly 81% for E_s/E_a = 5 and 136% for E_s/E_a = 100.

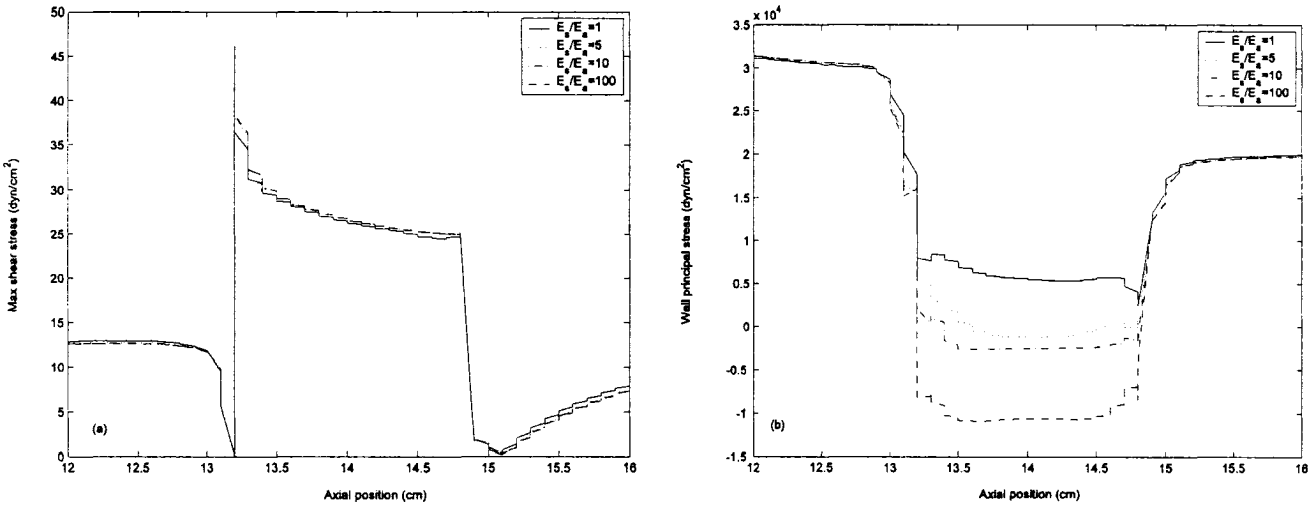

Figure 4.14 Fluid wall shear stress (a) wall principal stress (b) for hs = 0.1 cm at $R_e = 620$, $t = 0.5$ s

4.2.2 Reynolds number effects

Figure 4.15 (a) and (b) display the wall displacements and the pressure variations respectively, for 0.1 cm thickness, $E_s / E_a = 100$ and $R_e = 1200, 920, 620$. The latter were obtained by setting the outlet pressure at $p_2 = 0$, 600, and 1800 dyn/cm^2 respectively. Increasing R_e has the largest effect on the flow in the distal portion of the stent/artery structure as shown in Figure 4.15 (b). When the pressure difference is small (lower R_e) both the inlet segment and outlet segment of the artery wall are deformed outward with respect to the stent but when the pressure difference is large (higher R_e), the distal portion of the artery experienced further area reduction that increased as the Reynolds number is increased. However, increasing R_e resulted in almost no change in the stented segment due to the higher stiffness. It is noted that in this work, the choice of the pressure values at the artery/stent system outlet had the largest effect on the shape of the distal portion of the artery in that, when R_e = 1200 (p_2 = 0) the pressure drop became quite large and, with the presence of the constricted area at the stent, much of the flow in the stent and in the distal portion of the artery is dominated by negative pressure values which are smaller than the outside pressure and hence the shape of the artery/stent system.

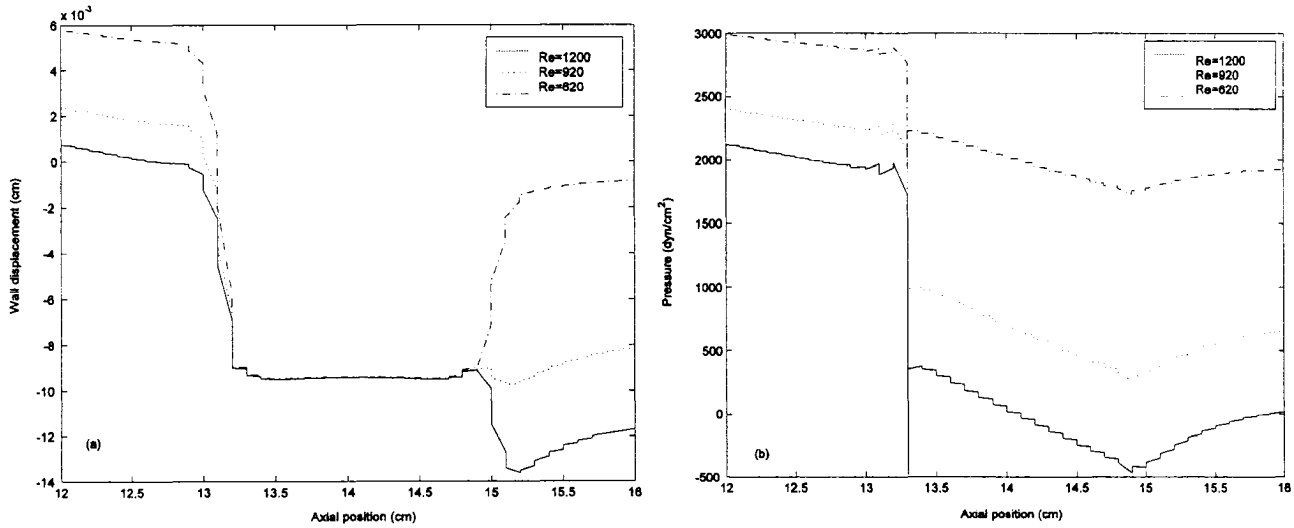

Figure 4.15 (a) Wall displacement (b) pressure variations for 0.1 cm thickness and $E_s / E_a = 100$.

The fluid wall shear stress and wall principal stress distributions for $R_e = 1200,\ 920,\ 620$, $E_s / E_a = 100$ and $t = 0.5$ are given in Figure 4.16 (a) and 4.16 (b) respectively. Generally, the increased Reynolds numbers only affected the magnitude of the fluid shear stress throughout the artery/stent system but not its axial variations as shown in Figure 4.16 (a). Evaluations of $\Delta\tau_w/\tau_{w,rf}$ at the stent inlet gave 177% and 261% for Re = 620 and 1200 respectively. The effects of increased Reynolds number on the wall principal stress is different from that of the fluid shear stress namely, the magnitude of the wall principal stress outside the stent decreased with increasing R_e but remained negative (compressive) and roughly unchanged within the stent. Estimates of the changes in the wall principal stress values at the proximal compliance mismatch zone, $\Delta\sigma_p / \sigma_{p,rf}$, gave 58% and had nearly the same values for all Re investigated here.

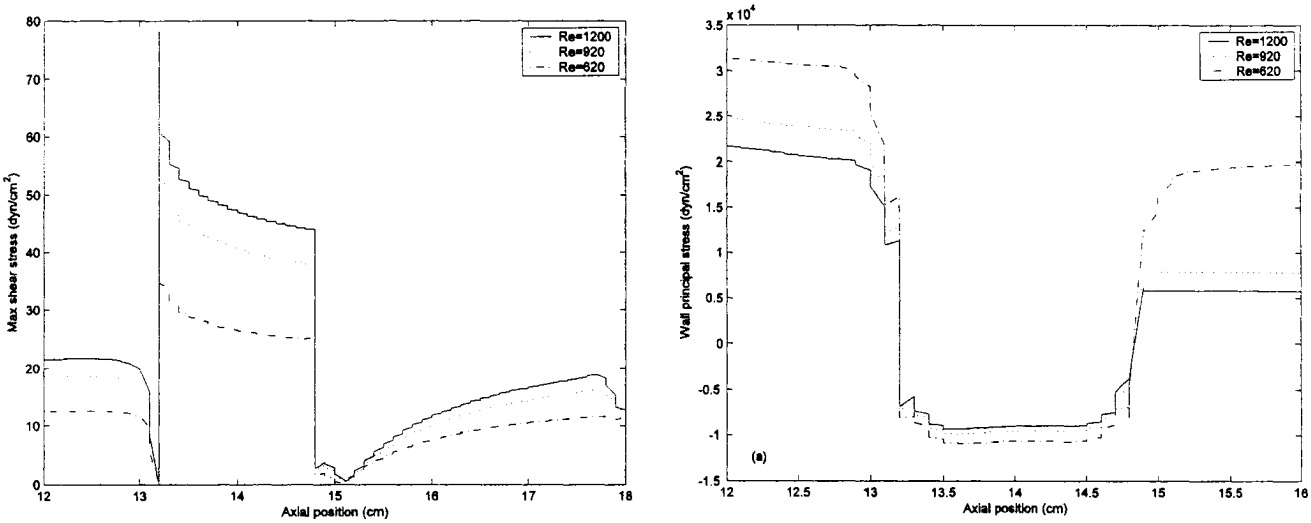

Figure 4.16: Fluid wall shear stress (a) Wall principal stress (b) for 0.1 cm thickness and $E_s / E_a = 100$, $t = 0.5$ s

Chapter 5 Analysis of the Results

In the present work the effects of the stent geometry and its compliance on the flow dynamics and wall mechanics of a stented artery when subjected to an inlet pulsatile pressure were numerically investigated. Two stent geometries were investigated; a stent that had the same wall thickness, hs, as the artery and a stent with a wall thickness of hs = 0.1 cm. In the absence of any reliable data on the elasticity of an in vivo stent in the literature, the elasticity of the stented part of the artery was varied from 1 to 100 times that of the main artery.

5.1 Flow and wall mechanical properties changes with stent elasticity

In this section, the stent that had the same wall thickness as the artery will be discussed. The main results of the effects of elasticity ratio and Reynolds number are summarized in Figures 5.1 and 5.2 respectively. The data plotted in Figure 5.1 suggest that the presence of a stented region within an artery resulted in small deformations of the arterial wall shape with no appreciable dependence on the stent stiffness and, as the stiffness of the stented artery increased, the arterial wall shape within the stented region became less time dependent. A pressure drop in the range of 1.2% and 1.6% was also observed within the stented region when hs = 0.04 cm. This fact suggests that the flow pressure was weakly dependent on the elasticity ratio. The wall shear stress was more sensitive to the flow changes and its value at the compliance transition zone increased as stiffness of the stent increased as shown in Figure 5.1. The wall shear stress at the compliance transition zone increased at a much faster rate at lower E_s/E_a. The increased stiffness of the stent had the largest effect on the wall principal stress as shown in Figure 5.1. For the stent with hs = 0.04 cm, the wall principal stress increased abruptly at the artery/stent joints and its value at those locations increased with increased stent stiffness. The wall principal stress

showed similar behaviour as the wall shear stress in that it increased much faster for the lower values of elasticity ratio.

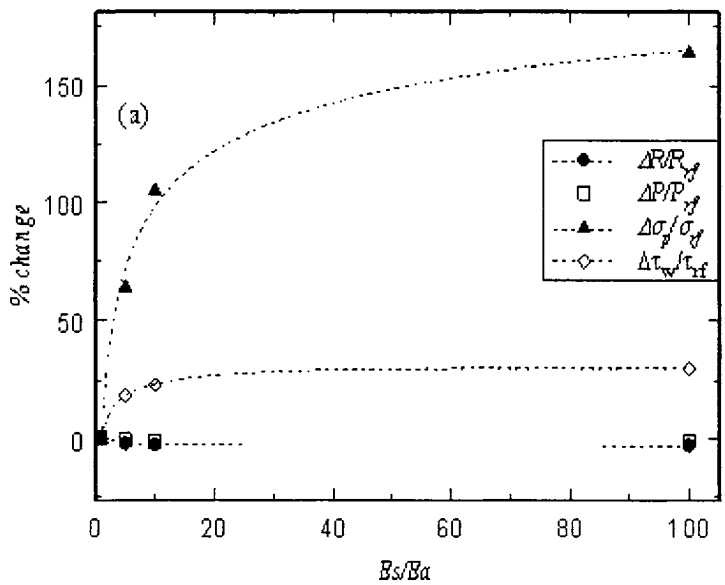

Figure 5.1: Changes in flow and wall mechanical properties at t = 0.5 s, hs = 0.04 cm.

Figure 5.2 shows the flow and wall mechanical properties changes as R_e changes when E_s/E_a = 5. It was seen in the previous Chapter that increasing R_e changed the pressure in field within the artery/stent system and, accordingly the whole artery/stent system wall shape changed as R_e increased. However, when the radius reduction was expressed as $\Delta R/R_{rf}$, the estimates gave values that were about 2.5% for R_e = 620 and decreased to 1.2% for R_e = 1200 suggesting that R_e had minor effects on the step size change at the stent inlet. The wall shear stress within the artery/stent system increased as R_e increased but, as shown in Figure 5.2, the change in magnitude across the stent inlet decreased as R_e increased. This can be explained by the fact that as R_e increased the step size change is smaller and hence smaller flow disturbance which results in lower wall shear stress magnitude change at the stent inlet. As was shown in the simulation results, the wall principal stress decreased with increasing R_e. Estimates of the changes in magnitude of the wall principal stress across the stent inlet was roughly constant of about 58% with no dependence on R_e as shown in Figure 5.2.

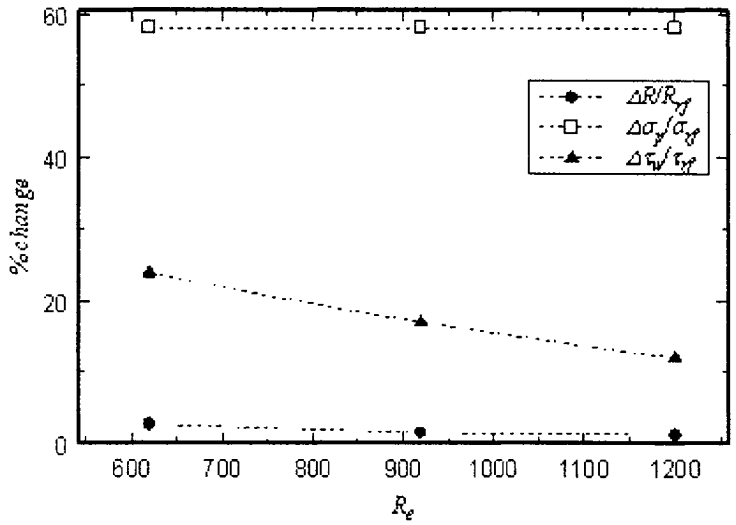

Figure 5.2: Changes in flow and wall mechanical properties at t = 0.5 s, hs = 0.04 cm, $E_s/E_a = 5$.

5.2 Flow and wall mechanical properties changes with stent geometry

Figures 5.3 and 5.4 display the flow and mechanical properties changes when hs = 0.1 cm. Here, the radius reduction for the undisturbed artery was evaluated to be 15% at the stent inlet. At the peak value of the pressure wave, the radius reduction was evaluated to be 16% when E_s/E_a = 1 and increased to 17% for all other values of E_s/E_a. The combination of stiffness increase and thickness increase of the stented part of the artery has only a minor effect on the wall shape of the artery/stent system as shown in Figure 5.3. This fact is in agreement with the estimated pressure drop across the stent inlet which was evaluated to be about 32% irrespective of the value of E_s/E_a as shown in Figure 5.3. This suggests that the flow pressure was, generally, affected by the stent geometry but weekly dependent on the elasticity ratio. The wall shear stress was more sensitive to the flow changes caused by in increased stent thickness in that its magnitude drastically increased to 280% at the compliance transition zone when the stent thickness increased to hs = 0.1 cm, with no appreciable dependence on the stent stiffness as shown in Figure 5.3. It can be concluded that the onset of a stent thickness that is larger than that of the artery, makes the wall shear stress behaviour to be controlled by the stent geometry and

not by the stent stiffness. As reporter in the previous Chapter, the increased thickness of the stent to hs = 0.1 cm has changed the behaviour of the wall principal stress when compared to case of hs = 0.04 cm. More specifically, the wall principal stress decreased at the stent inlet and, for any given elasticity ratio, it retained the same magnitude throughout the stented portion of the artery. As shown in Figure 5.3, the wall principal stress decreases much faster for the lower values of elasticity ratio and became compressive when $E_s/E_a > 5$.

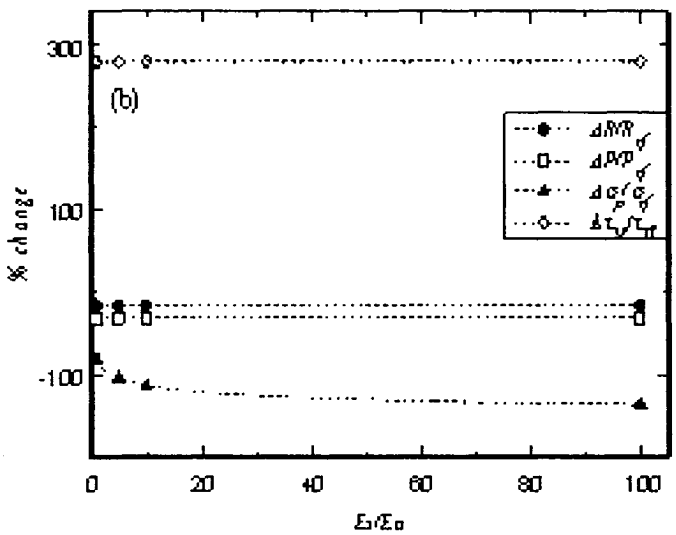

Figure 5.3: Changes in flow and wall mechanical properties at t = 0.5 s, hs = 0.1 cm.

The effects of increasing R_e, for the case of a stent with hs = 0.1 cm and E_s/E_a = 5, on the flow and mechanical properties are shown in Figure 5.4. The wall radius changes across the stent inlet show the same behaviour as for the case of hs = 0.04 cm. As seen in figure 5.4, $\Delta R/R_{rf}$ remained nearly constant (16% to 17%) irrespective of R_e values. The effect of increased R_e is more pronounced for the wall shear stress. As shown in Figure 5.4, the change in wall shear stress at the stent inlet increases as R_e increases. This can be explained by the fact that increasing R_e would results in a steeper wall pressure gradient at the stent inlet which in turn results in a larger increase in the wall shear stress at that location. Finally, the wall principal stress displays the expected dependence on R_e. Increasing R_e resulted in a lower pressure within the whole artery/stent system as

discussed in the previous Chapter and therefore, the principal stress decreases as R_e increases as shown in Figure 5.4.

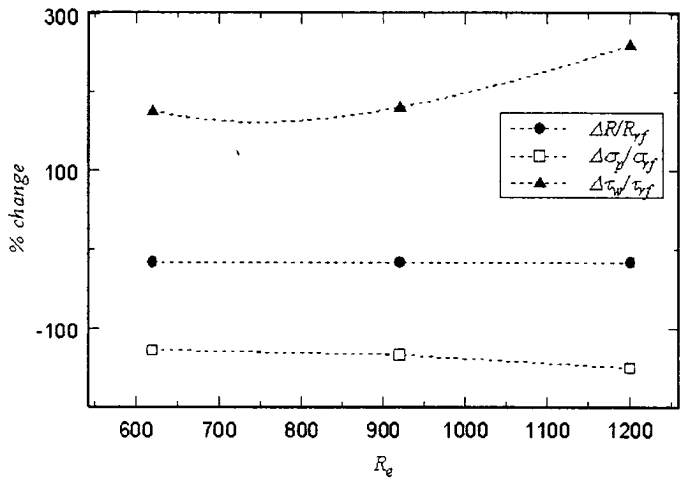

Figure 5.4: Changes in flow and wall mechanical properties at t = 0.5 s, hs = 0.1 cm, E_s/E_a = 5

5.3 Implications

It has long been established that high wall shear stress and low pressure are closely related to cell residence time and adhesion. From the local hemodynamic point of view, the present results suggested that the stent stiffness had only minor effects on the wall shape as well the pressure distribution within the artery/stent system. The flow pressure was largely affected by increasing the stent thickness which resulted in large wall pressure gradients at the compliance transition zones and low pressures within the stent which may lead to increased residence time and hence in-stent restenosis. Furthermore, the present results suggested that both stent stiffness as well as its thickness had large effects on the wall shear stress and wall shear stress values as high as 280% τ_{rf} at compliance transition region which may alter the mechanism of cell adhesion and potentially be the main reason of in-stent restenosis. The wall principal stress was also affected by both the thickness as well as the stiffness of the stent. The simulations have shown that the wall shear stress remained oscillating even for the case of E_s/E_a = 100 and

had increased by as much as 160% which may lead to stent fatigue and failure at the compliance transition zones.

Chapter 6 Experimental Setup and Future Work

To obtain a better understanding of pulsatile flow in stented arteries, a natural continuation of this study will be an experimental study. The first step to accomplish this goal is to develop an experimental setup that is capable of emulating a pulsatile flow in a scale-up stented artery. This Chapter describes the design and a preliminary test of an experimental setup built at Lakehead University.

6.1 Experimental setup

6.1.1 The dimensional analysis and experiment parameter

Because the dimensions of a real stented artery are very small, the experimental model has to be scaled up. A dimensional analysis was conducted to determine the dimensions of a test model. For any given geometric parameter, $\ell_{exp,i}$, of the test model must satisfy the condition given by:

$$\frac{\ell_{\exp,i}}{\ell_{\exp,j}} = \frac{\ell_{sim,i}}{\ell_{sim,j}} \tag{6-1}$$

where $\ell_{sim,i}$ stands for the corresponding geometric parameter pertaining to the model used in the ADINA simulations.

Dynamic similarity requires that Reynolds number, R_e, and Womersly number, α, must be the same for both the experimental model and the ADINA simulations. Mathematically, this condition is expressed as:

$$R_{e,\exp} = \frac{D_{\exp} \cdot \overline{U}_{\exp}}{\nu_{\exp}} = R_{e,sim} = \frac{D_{sim} \cdot \overline{U}_{sim}}{\nu_{sim}}$$

$$\alpha_{\exp} = \frac{D_{\exp}/2}{\sqrt{\nu_{\exp}/\omega_{\exp}}} = \alpha_{sim} = \frac{D_{sim}/2}{\sqrt{\nu_{sim}/\omega_{sim}}} \tag{6.2}$$

where, D is the diameter, $\bar{U}$ is the average flow speed, ν is the kinematic viscosity and ω is the flow pulsation frequency. The first equation in Eq. (6.2) was used to determine the required flow rate in the test section and the second was used to estimate the experimental pulsation frequency.

6.1.2 Apparatus

A schematic diagram of the developed experimental system is shown in Figure 6.1. The apparatus consists of a sump tank, a supply pump, a constant head supply tank, a programmable pump, a test section, a flow-meter and several manual valves. The supply pump (MINIVAC utility pump) delivers the water to the constant head tank which has an overflow tube to ensure a constant head. The programmable pump is a Masterflex L/S line of peristaltic pump which provides a pulsatile flow to the test section. The test section consists of a silicone tube 0.305 m long with 0.0127 m inside diameter located in a vertical position. An in-line flow-meter is used to measure instantaneous flow rate. All globe valves are used to create a blockage of pressure in the tube. The maximum flow rate is set as 2000 ml/min @600 rpm for the programmable pump. A photo of the actual experimental apparatus is shown in Figure 6.2.

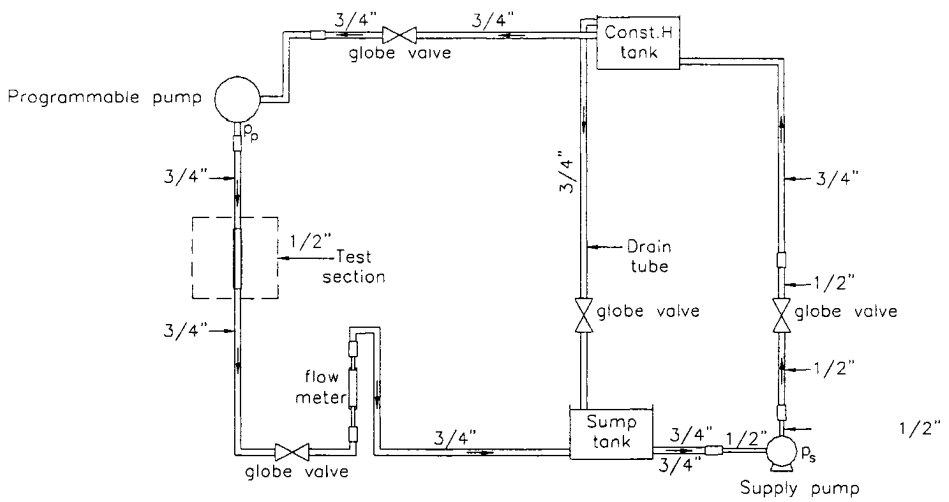

Figure 6.1 Schematic diagram of the closed flow loop experimental apparatus

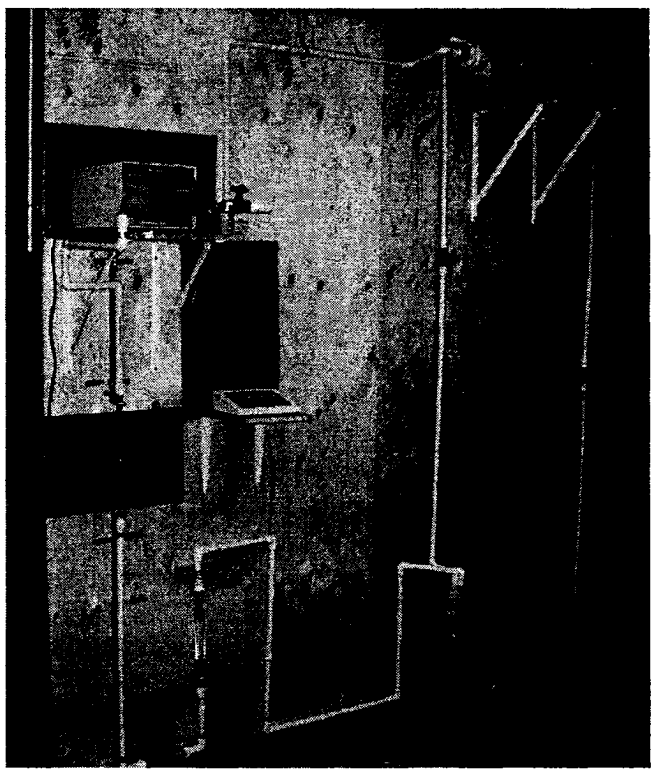

Figure 6.2 Photo of the experimental apparatus

6.2 Preliminary test

A preliminary test was conducted. Figures 6.3 to 6.6 are the photos of the testing tubing taken at the different conditions. Figure 6.3 shows the initial shape of the testing tube when the pressure in the pipe was set to be low. The pressure of the pipe is controlled by adjusting the valve before the flow meter. A 1.5 inch long steel tube is placed in the middle of the tube to model a stented artery. Figure 6.4 shows the shape of the testing tube when the flow rate is 2000 ml/min and the pressure was increased by adjusting the control valve. Figures 6.5 and 6.6 show the lower part of the tube and the middle part of the tube, respectively. From the pictures, we can see that with the increase in the pressure, the tube deforms. It is noted that the significant deformation occurs at the proximal and distal ends of the steel segment and the lower end of the testing tube. The results qualitatively match the simulation results, but not quantitatively. Also, due to the limit of the programmable pump, the pulsating effect is hardly observable.

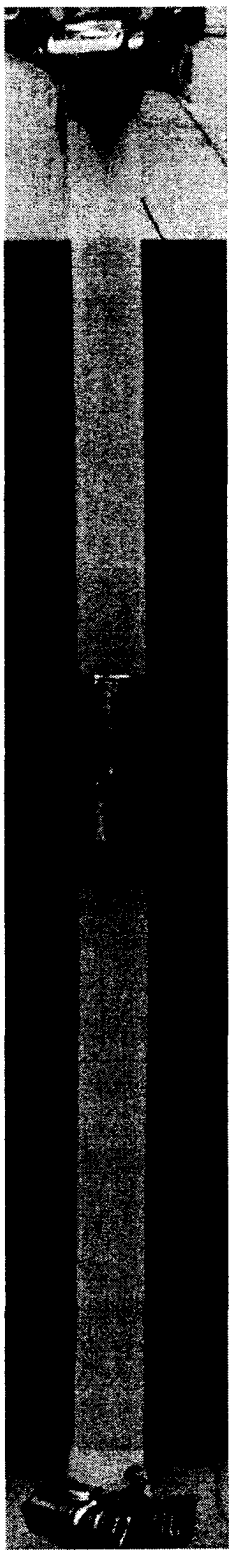

Figure 6.3 The initial shape of the testing tube

Figure 6.4 The shape of the testing tube when the flow rate is 2000 ml/min.

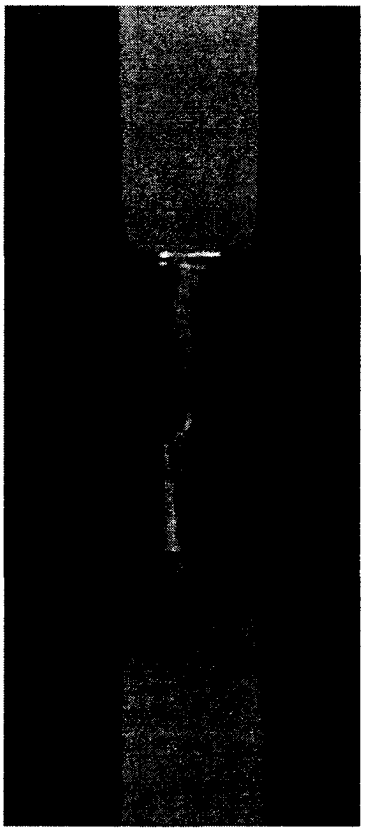

Figure 6.5 The middle part of the deformed tube when the flow rate is 2000 ml/min

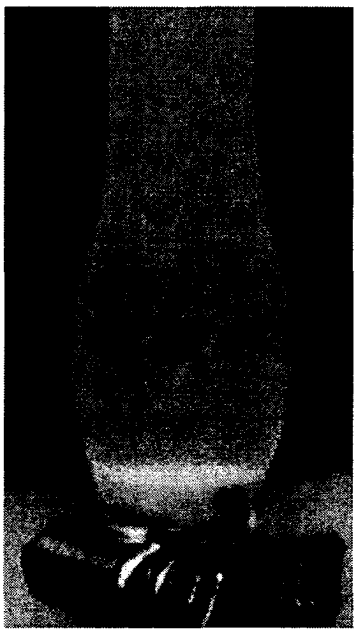

Figure 6.6 The lower end of the deformed tube when the flow rate is 2000 ml/min

6.3 Future work

As a first step towards experimentally studying the interactions between a pulsatile flow and a stented artery, the experimental setup discussed above was built as part of the present work. The selected components seem to have achieved the required flow criteria except the setup should include a means by which the flow entering the test section can be determined. This is important especially that the flow exiting the programmable pump encounters a number of flow bends that potentially may alter the flow pressure time variations. The material properties for stent should be selected such that a variety of stent stiffness can be experimentally determined. The simulations discussed in the previous Chapters have shown that the arterial wall displacement with respect to the undisturbed tube wall were of the order of 0.1 mm very small to be measured by conventional means. A special rig should be conceived to be able to detect the tube wall displacement at frequencies that are at least 5 to 10 times faster than the pulsation frequency of the programmable pump.

Chapter 7 Conclusions and Recommendations

7.1 Conclusions

We have used ADINA to build a stented artery model. The model describes a fully coupled fluid-structure interaction of such a system. Using the model, we have investigated the effects of compliance mismatch on blood flow and influence of the artery/stent geometric parameters and wall elasticity on hemodynamics and artery wall mechanics. Based on the four cases investigated, the study results are summarized as follows.

- *A stented artery with a uniform wall thickness and a constant Reynolds number*

With a uniform wall thickness, compliance mismatch causes non-uniform wall deformation. The deformation unevenness at the stent inlet defined by $\Delta R/R_{rf}$ is found to be 2.5% and 3.3% for E_s/E_a = 5 and E_s/E_a = 100 respectively. The change in the wall deformation in the stent region results in the uneven pressure drop as well. The pressure change defined by $\Delta P/P_{rf}$, is found to be 1.2% and 1.6% for E_s/E_a = 5 and E_s/E_a = 100 respectively. The wall principal stress experiences a sharp increase right at the compliance transition zone. The increase in the wall principal stress defined by $\Delta\tau_p/\tau_{p,rf}$ is found to be 64% and 164% for E_s/E_a = 5 and 100 respectively. This finding suggests that the compliance mismatch causes a stress concentration at the stent inlet and outlet. The fluid shear stress on the other hand, is marked by a sharp increase at the stent inlet but sharply decreases at the stent outlet.

- *A stented artery with a uniform wall thickness and different Reynolds numbers.*

The unevenness in the wall deformation is more significant when the Reynolds number is low than that when the Reynolds number is higher.

- *A stented artery with a non-uniform wall thickness and a constant Reynolds number.*

The wall deformation, $\Delta R/R_{rf}$ is 16% and 17% for E_s/E_a = 1 and 5, respectively. The value $\Delta R/R_{rf}$ remains almost unchanged when E_s/E_a increases further. This suggests that the wall thickness increase has the same effect as the compliance mismatch. Observation of the flow pressure behavior suggests that the flow pressure is, generally, affected by the stent geometry but weekly dependent on the elasticity ratio. The fluid shear stress generally exhibits an axial variation that resembled the uniform wall thickness case except that it displays mach larger peak values at the stent inlet and outlet. Also, it drops to zero values just ahead and downstream of the stent due to the presence of the separated flow at those regions. The wall shear stress change at the stent inlet, $\Delta\tau_w/\tau_{w,rf}$ is estimated to be 260% irrespective of the elasticity ratio. However, the wall principal stress exhibits a behaviour that is quite distinct from that of the uniform wall thickness case.

- *A stented artery with a non-uniform wall thickness and different Reynolds number.*

When the pressure difference is small (lower R_e) both the inlet segment and outlet segment of the artery wall are deformed outward with respect to the stent but when the pressure difference is large (higher R_e), the distal portion of the artery experiences further area reduction that increases as the Reynolds number increases. The increased Reynolds numbers only affect the magnitude of the fluid shear stress throughout the artery/stent system but not its axial variations. The wall shear stress experiences a sharp increase at both the stent inlet and outlet. The higher the pressure difference, the larger the shear stress concentration. The effects of increased Reynolds number on the wall principal stress is different from that of the fluid shear stress namely, the magnitude of the wall

principal stress outside the stent decreased with increasing R_e but remained negative (compressive) and roughly unchanged within the stent.

7.2 Recommendations

This study can be furthered in the following directions.

- Although the 2-D axisymmetrical model used in this study captures the essence of the stented artery, the model is a simplified one. To closely represent the real system, a three-dimensional model is needed. With a 3-D model, effects of various mechanical forces involved can be better understood. For example, the stress/strain relationship in circumferential direction will be considered in the 3-D model. The detailed patterns of the stent geometry can be modeled. The stent in an asymmetric stenosis can be studied. A 3-D model will also allow the study of stent design.

- The present experimental system needs further improvements in order to carry out an experimental study. The following works need to be done. A more powerful programmable pump is needed in order to generate a pulsating flow that can induce more visible tube deformation. A more reliable measurement means for the wall deformation is needed. An effective way to observe the flow pattern in the testing tube is required.

7.3 Potential in Control Applications

In the future, an active control stent may offer a better solution to in-stent restenosis. Understanding of stent/artery/blood interaction is essential to the development of such active control stents. Presently, there have been two promising developments:

- Drug-eluting stent can deliver drug to heal the injury caused by insertion of stent.

- Smart (Shape Memory Alloy Recoverable Technology) stent possesses recoverability that opposes any external deforming force with a higher 'springback' force, quickly reassuming its expanded shape to maintain the integrity of the lumen it supports.

An active stent is expected to be capable of accomplishing aforementioned tasks and more such as adaptability to changing environments.

Bibliography

H. Alderson and M. Zamir, Effects of stent stiffness on local haemodynamics with particular reference to wave reflections. J Biomechanics, Vol.37 (2004), 339-348.

M. Bathe, R.D. Kamm, A fluid-structure interaction finite element analysis of pulsatile blood flow through a compliant stenotic artery, J Biomech Eng, Vol.121 (1999), 361-369.

J.L. Berry, E. Manoach, C. Mekkaoui, P.H. Rolland and J.E. Moore, Hemodynamics and wall mechanics of a compliance matching stent: In vitro and in vivo analysis. J Vasc Interv Radiol , Vol.13 (2002), 97-105.

V. Deplano and M. Siouffi, Experimental and numerical study of pulsatile flows through stenosis: Wall shear stress analysis. J Biomech Eng, Vol.32 (1999), 1081-1090.

P. H. Grewe, T. Deneke, A. Machraoui, J. Barmeyer, K. M. Muller, Acute and chronic tissue response to coronary stent implantation: pathologic findings in human specimens. Journal of the American College of Cardiology, Vol.35 (2000), 157-163.

T.W. Lowe and T.J. Pedley, Computation of stokes flow in a channel with a collapsible segment. Journal of Fluids and Structures, Vol.9 (1995), 885-905.

X.Y. Luo and T.J. Pedley, A numerical simulation of steady flow in a 2-D collapsible channel. Journal of Fluid and Structure Vol.9 (1995), 149-174.

X.Y. Luo and T.J. Pedley, A numerical simulation of unsteady flow in a two-dimensional collapsible channel. Journal of Fluid Mech Vol.314 (1996), 191-225.

Z. Mohammad, J.E. Moore Jr., J.L. Berry, E. Manoach and A. Rachev, Effects of compliance transitioning on wall stresses in a stented artery. Mechanical Engineering Department, Florida International University.

J.E. Moore and J.L. Berry, Fluid and mechanical implications of vascular stenting. Annals of Biomech Eng, Vol.30 (2002), 498-508.

F. Nicoud, Hemodynamic changes induced by stenting in elastic arteries. Center for turbulence research, Annual research briefs (2002).

G. Pedrizzetti, F. Domenichini, A. Tortoriello and L. Zovatto, Pulsatile flow inside moderately elastic arteries, its modeling and effects of elasticity. Computer methods in Biomechanica and Biomedical Eng, Vol.5 (3) (2002), 219-231.

G. Pontrelli, Modeling the fluid-wall interaction in a blood vessel. Biomedical Research (2001).

Z.D. Shi, S.H. Winoto and T.S. Lee, Experimental investigation of pulsatile flows in tubes. Journal of Biomechanical Engineering Vol.119 (1997), 213-216.

I. Surovtsova, Effects of compliance mismatch on blood flow in an artery with endovascular prosthesis. J Biomechanics, Vol.38 (2005), 2078-2086.

M. Siouffi, V. Deplano, R. Pelissier, Experimental analysis of unsteady flows through a stenosis. J Biomechanics, Vol.31 (1998), 11-19.

D. Tang, C. Yang, S. Kobayashi and D.N. Ku, Effect of a lipid pool on stress/strain distributions in stenotic arteries: 3-D fluid-structure interactions (FSI) models. J Biomech Eng, Vol.126 (2004), 363-370.

D. Tang, C. Yang, J. Zheng, P.K. Woodard, G.A. Siicard, J.E. Saffitz and C. Yuan, 3D MRI-based multicomponent FSI models for atherosclerotic plaques. Annals of Biomech Eng, Vol.32 (2004), 947-960.

D. Tang, C. Yang, S. Kobayashi, J. Zheng and R.P. Vito, Effect of stenosis asymmetry on blood flow and artery compression: A three-dimensional fluid-structure interaction model. Annals of Biomech Eng, Vol.31 (2003), 1182-1193.

D. Tang, C.Yang, H. Walker, S. Kobayashi and D.N. Ku, Simulating cyclic compression using a 3D unsteady model with fluid-structure interactions. Computers & structures, Vol.80 (2002), 1651-1665.

D. Tang, C. Yang and D.N. Ku, A 3-D thin-wall model with fluid-structure interactions for blood flow in carotid arteries with symmetric and asymmetric stenoses. Computers & structures, Vol.72 (1999), 357-377.

D. Tang, C. Yang, Y. Huang and D.N. Ku, Wall stress and strain analysis using a three-dimensional thick-wall model with fluid-structure interactions for blood flow in carotid arteries with stenoses. Computers & structures, Vol.72 (1999), 341-356.

D. Tang, J. Yang, C. Yang and D.N. Ku, A nonlinear axisymmetric model with fluid-wall interactions for steady viscous flow in stenotic elastic tubes. Transaction of the ASME, Vol.121 (1999), 494-501.

D. Theodoros G. Papaioannou, C. Stefanadis, Vascular shear stress: Basic principles and methods. Hellenic Journal of Cardiology, Vol.46 (2005), 9-15.

A. Tortoriello and G. Pedrizzetti, Flow-tissue interaction with compliance mismatch in a model stented artery. J Biomechanics, Vol.37 (2004), 1-11.

H. Zhang, X. Zhang, S. Ji, Y. Guo, G. Ledezma, N. Elabbasi and H. deCougny, Recent development of fluid-structure interaction capabilities in the ADINA system. Computers & Structures, Vol.81 (2003), 1071-1085.

Appendix

Fluid–Structure Interaction Capabilities of the ADINA System

A.1 Introduction

The computation of fully coupled fluid flows with structure interactions is a rapidly devolving discipline that has been given increased attention in recent years. Traditional fluid flow solutions are obtained by assuming a given motion of the structure that bounds the fluid; and structural solutions are typically obtained by prescribing properties (typically pressure) to the fluid that abuts the solid. Sometimes, iterations between the fluid and structural media are manually performed in order to ensure that reasonable assumptions have been made. However, there are many problems where a fully coupled analysis is needed in order to model the fluid-structural interaction (FSI). This is particularly important when the structure undergoes large deformations resulting from the present of the fluid. With the recent advances in mathematical models and their associated numerical methods, the accurate analysis of such fully coupled system is now possible.

The ADINA system is a general-purpose finite element and finite volume code for the analysis of structures, fluid flows and fluid-structure interactions. Fluid flows can be modeled as Navier-Stokes incompressible, slightly compressible, and fully compressible. They can be 2D planar, 2D axisymmetric or 3D. Structures can be modeled as 2D/3D solids, beams or shells. The fluid and structure can be coupled through their interface. In order to handle the moving interface between fluids and solids, an arbitrary Lagrangian-Eulerian (AEL) formulation can be applied to the fluid. Both iterative and direct solution procedures can be used for solving the fully coupled system. These capabilities, together with the extensive boundary conditions and material models, and the user-friendly graphical system for pre-and post-processing (AUI), make the ADINA system a powerful tool for engineers and researchers.

The purposes of this section are twofold: examination of the FSI capabilities of the ADINA and familiarization of the ADINA FSI modeling procedure. To this end, we use three examples: a steady fluid flow in a rigid tube, a pulsatile flow in a rigid tube, and a pulsatile flow in a 2-D collapsible channel.

A.2 Dynamics analysis of a steady fluid flow in a tube

This study uses an ADINA model to investigate the behaviors of a fully developed laminar flow in a rigid tube and compare the results with the theoretical solutions. It shows that there is a good agreement between the ADINA results and the theoretical solutions.

A.2.1 The model

The problem under consideration is shown in Figure A.1. The following assumptions are made:

- The flow is steady and laminar.
- The fluid is incompressible, Newtonian and viscous.

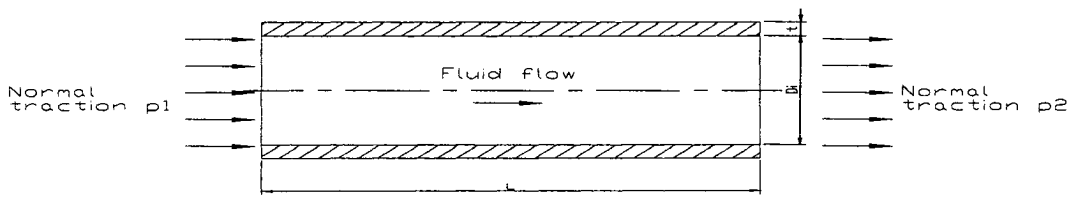

Figure A.1. A tube conveying a laminar flow

The geometric parameters are listed below:

Tube radius: $R = 0.005\ m$

Tube length: $L = 1.5\ m$

The physical parameters are listed below

Dynamic viscosity: $\mu = 1 \times 10^{-3}$ N-s$/m^2$

Fluid density: $\rho_f = 1000$ kg$/m^3$

Inlet pressure: $p_1 = 87\ Pa$

Outlet pressure: $p_2 = 0$

A.2.2 Finite element modeling

In the ADINA model built, the $r \times \theta \times z$ mesh used for the subdivision was $32 \times 20 \times 4$. Also set the "Length Ratio of Element in w-direction" to 0.5. The fluid was modeled with 4-nodes per elements. Element type used was 3-D fluid. The inlet and outlet pressures were imposed using the 'normal traction' option.

A.2.3 ADINA results

Table A.1 shows the flow rate, average velocity, and maximum velocity of the flow at different axial positions. The results show that all the eight quantities are constant along the axial direction. Also the maximum velocity almost is twice time as the average velocity. The results are very close to the theoretical values (see below the calculations).

Table A.1. The flow rate, average and maxima velocities of the fluid of eight axial positions

Position (L)	Total volume flux (Q)	Average velocity ($\bar{V}$)	Max. velocity (V_{max})
0.1	1.38×10^{-5}	1.769×10^{-1}	3.69×10^{-1}
0.3	1.38×10^{-5}	1.769×10^{-1}	3.717×10^{-1}
0.5	1.38×10^{-5}	1.7687×10^{-1}	3.729×10^{-1}
0.7	1.38×10^{-5}	1.7687×10^{-1}	3.736×10^{-1}
0.9	1.38×10^{-5}	1.7688×10^{-1}	3.739×10^{-1}
1.1	1.38×10^{-5}	1.7686×10^{-1}	3.742×10^{-1}
1.3	1.38×10^{-5}	1.7686×10^{-1}	3.743×10^{-1}
1.5	1.38×10^{-5}	1.769×10^{-1}	3.754×10^{-1}

A.2.4 Theoretical results

For the steady laminar flow in a tube, the volume flow rate is found by integrating the velocity profile over the cross-sectional area:

$$Q = \iint_A V_x dA = \int_0^{2\pi}\int_0^R \frac{R^2}{4\mu}\left(-\frac{dp}{dx}\right)\left[1-\left(\frac{r}{R}\right)^2\right] r dr d\theta \qquad \text{(A.1)}$$

Integrating the above equation results in

$$Q = \frac{\pi R^4}{8\mu}\left(-\frac{dp}{dx}\right) \qquad \text{(A.2)}$$

In a fully developed flow, the volume flow rate is further given by

$$Q = \frac{\pi R^4 \Delta p}{8\mu L} \qquad \text{(A.3)}$$

Substituting the given values in Eq. (A.3) yields the theoretical flow rate

$$Q = \frac{\pi \times 0.005^4 \times 87}{8 \times 1.0 \times 10^{-3} \times 1.5} = 1.42 \times 10^{-5} \text{ m}^3/\text{s}$$

which is close to the numerical results in Table A.1. The average velocity is

$$V = \frac{Q}{A} = \frac{R^2 \Delta p}{8 \mu L} = \frac{0.005^2 \times 87}{8 \times 1.0 \times 10^{-3} \times 1.5} = 1.81 \times 10^{-1} \text{ m/s} \tag{A.4}$$

which is close to the numerical results in Table A.1. The maximum velocity is

$$U_{\max} = \frac{R^2 \Delta p}{4 \mu L} = 2\bar{V} = 3.62 \times 10^{-1} \text{ m/s} \tag{A.5}$$

which is close to the numerical results in Table A.1. For the fully developed laminar flow in a tube, the velocity profile takes a parabolic shape given by

$$\frac{u}{U_{\max}} = 1 - \left(\frac{r}{R}\right)^2 \tag{A.6}$$

The shear stress is given by

$$\tau_{rx} = \mu \frac{du}{dr} = \frac{r}{2}\left(\frac{dp}{dx}\right) \tag{A.7}$$

On the wall, the shear stress, τ_w is given by

$$\tau_w = -\left[\tau_{rx}\right]_{r=R} = \frac{R \Delta p}{2L} = \frac{0.005 \times 87}{2 \times 1.5} = 0.145 \text{ N/m}^2 \tag{A-8}$$

Table A.2 The axial velocity profile over a cross-section

r (m)	u (m/s)
-5×10^{-3}	0
-4.1449×10^{-3}	1.1352×10^{-1}
-3.0676×10^{-3}	2.247×10^{-1}
-1.7102×10^{-3}	3.162×10^{-1}
0	3.673×10^{-1}
1.7102×10^{-3}	3.162×10^{-1}
3.0676×10^{-3}	2.247×10^{-1}
4.1449×10^{-3}	1.1352×10^{-1}
5×10^{-3}	0

Figure A.2 compares the velocity profile from ADINA and that from Eq. (A.6). Figure A.3 compares the normalized velocity profiles where the results from ADINA are divided by its maximum value.

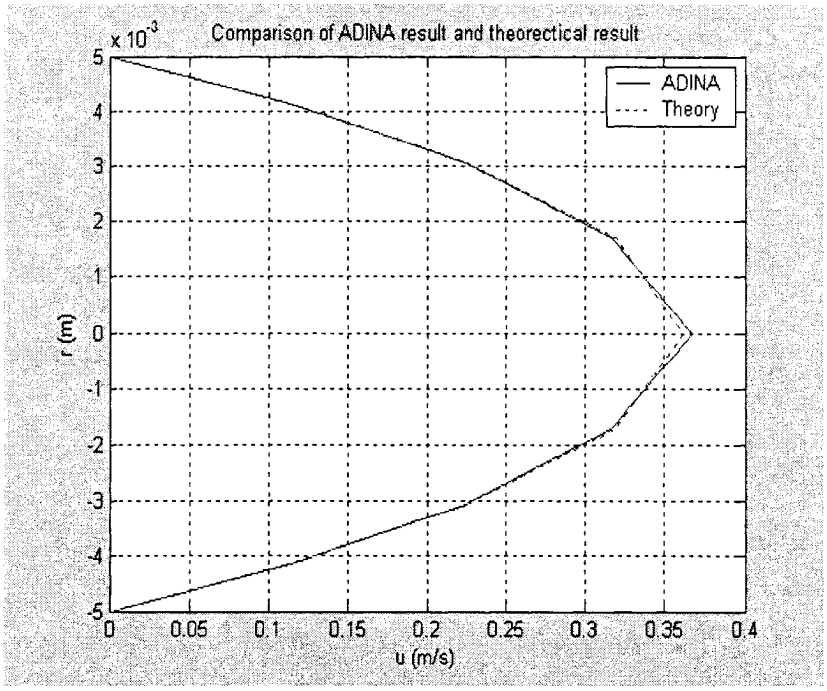

Figure A.2. Comparison of the absolute velocity profiles

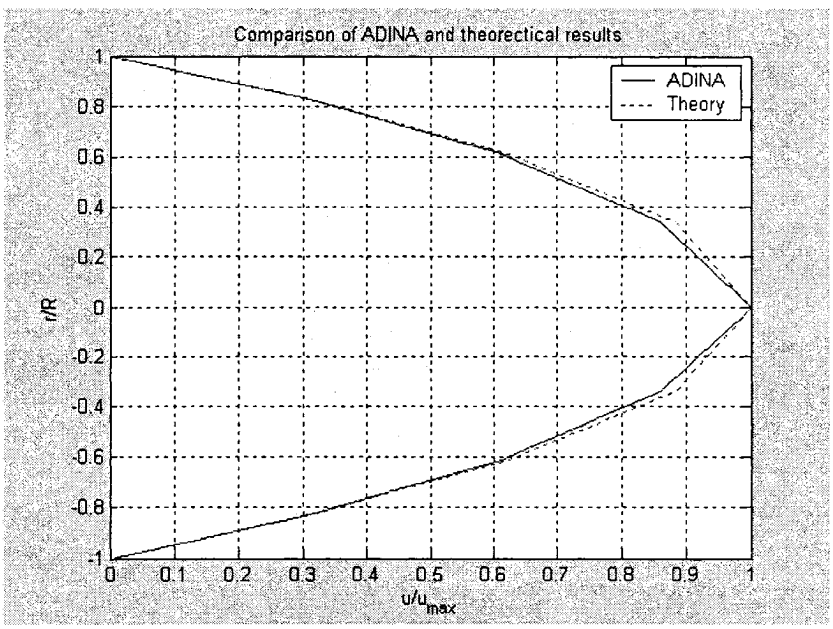

Figure A.3. Comparison of the normalized velocity profiles

A.3 Investigation of a pulsatile flow in a rigid tube

An experimental investigation of a pulsatile flow in a circular rigid tube was performed by Adamec et al. (2001). The purpose of this section is to use ADINA to model the same problem and compare the ADINA results with those given in their report.

A.3.1 The model

The tube under consideration is shown in Figure A.4. The following assumptions are made:

- The flow is unsteady and laminar.
- The fluid is incompressible, Newtonian and viscous.

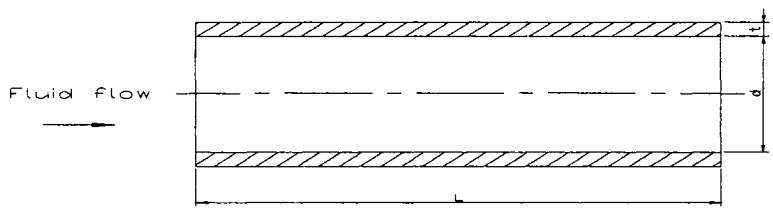

A.4. A tube conveying a laminar flow

The geometric parameters are listed below:

Tube diameter: $d = 0.02$ m

Tube length: $L = 2$ m

The physical parameters are listed below:

Dynamic viscosity: $\mu = 1 \times 10^{-3}$ N-s/m^2

Fluid density: $\rho_f = 1000$ kg/m^3

The pulsatile flow is characterised by the following equation:

$$Q = Q_s(1 + \lambda \sin(\omega t)) \tag{A.9}$$

where Q_s is the stationary component of the volume flow rate, $\lambda = Q_{pm}/Q_s$ with Q_{pm} representing the maximum amplitude of the oscillatory component of the volume flow rate, ω is the angular frequency of oscillation which is defined by Wormersley number $\alpha = d/2\sqrt{\omega/\nu}$ where ν is kinematical viscosity. In this study, we specify the following parameters:

$Q_s = 1$ $l/\min$ and $Q_s = 2$ $l/\min$, $\alpha = 11$ and $\lambda = 0.9$

Then

$$\omega = (\frac{2\alpha}{d})^2 \nu = (\frac{2 \times 11}{0.02})^2 \times 10^{-6} = 1.21 \text{ rad/s} \tag{A.10}$$

The fluid velocity is given by:

$$V = \frac{Q}{A} = 0.053(1 + \lambda \sin 1.21t) \tag{A.11}$$

A.3.2 Finite element modeling

In the ADINA model built, the $r \times \theta \times z$ mesh used for the subdivision was $12 \times 16 \times 6$. Also set the "Length Ratio of Element in w-direction" to 0.5. The fluid was modeled with

4-nodes per elements. Element type used was 3-D fluid. The pulsatile velocity was defined as a time function. We tried several ways. First, we started Eq. (A.11) at $t=0$ with a time step $\Delta t=0.15$ s. We found that the results for the first time step were unreasonable. Then we followed Problem 30 in Primer. We set $V=0$ at $t=0$ and $V=0.053$ m/s at $t=1$ s. Then we started Eq. (A.11) from $t=1$ s. This way, the results seem to be reasonable.

Figure A.5 shows the tube and the mesh used in the computation

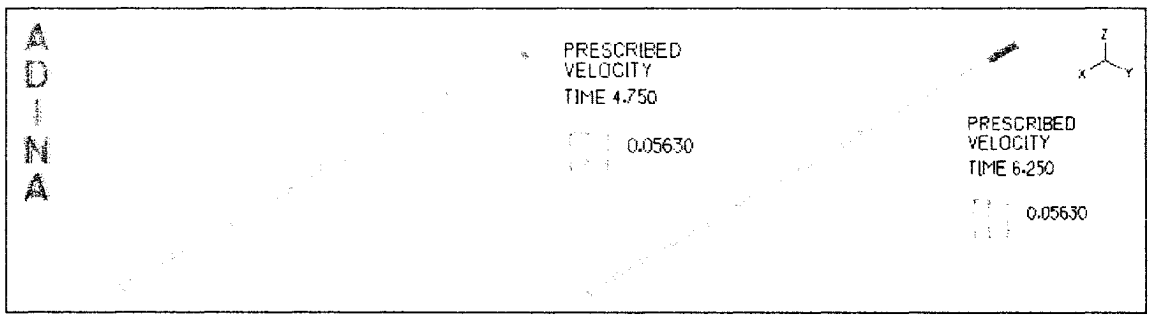

Figure A.5. The mesh used in ADINA

A.3.3 ADINA results

Values of instantaneous velocity depend on radial position of the tube. Figure A.6 show the velocity vs time at $r=0.0072$ m from the axis of the tube. Figure A.7 is the same velocity vs. degree. The maximum velocity is 0.124 m/s for $Q_s=1\ l/\min$ and 0.248 for $Q_s=2\ l/\min$ which very close to the experimental result. Figure A.8 gives the velocity profiles of several axial locations at certain time. We can see the velocity profiles are same at every cross section. It has been found that the ADINA results agree well with the experimental ones.

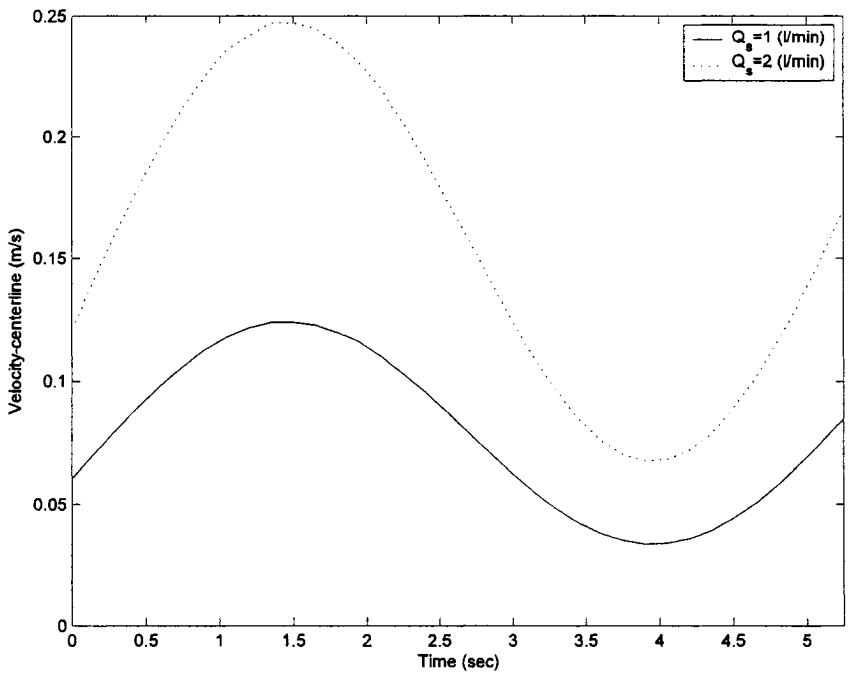

Figure A.6. Velocity profile vs time at $r = 0.0072$ m, for $\alpha = 11$, $\lambda = 0.9$

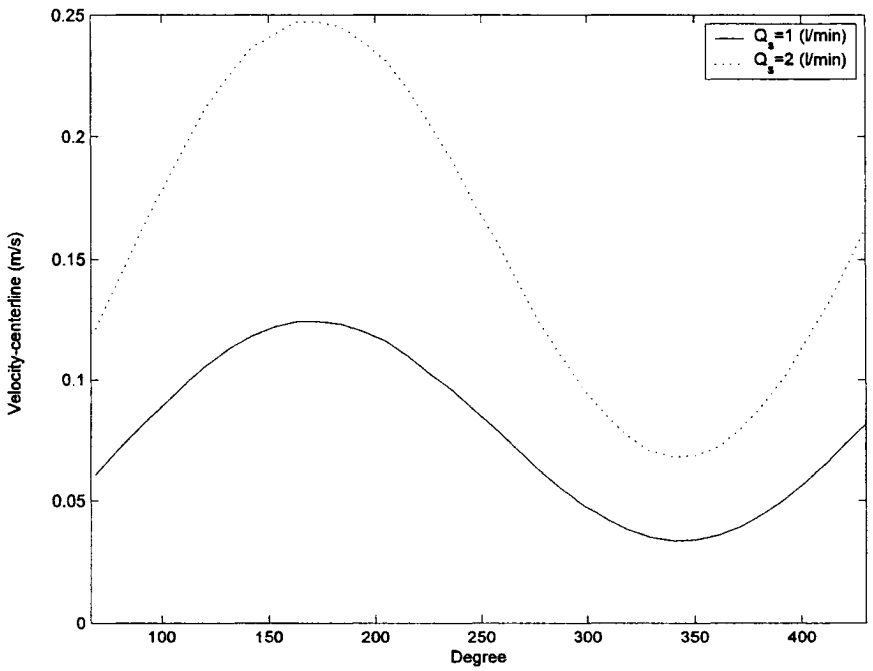

Figure A.7. Instantaneous velocity vs degree for $\alpha = 11$, and $\lambda = 0.9$

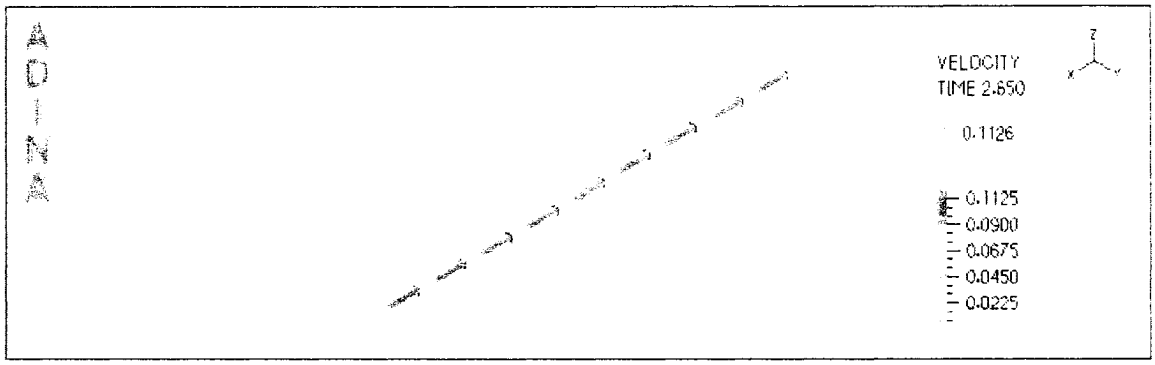

Figure A.8. Velocity profiles at several axial locations

A.4 Investigation of an unsteady flow in a 2-D collapsible channel

This example involves an unsteady flow in a two-dimensional (2-D) collapsible channel. The problem has been considered to be a typical fluid-structure interaction which has been studied by many researchers in numerical investigation (X.Y.Luo and T.J.Pedley 1996-1998). The applications for such a model include fluid flow in deformed arteries. We will use ADINA to solve the problem.

A.4.1 The model

The model consists of two parts, an ADINA (solid) model and an ADINA-F (fluid) model which is shown in Figure A.9. Due to fluid forces causing structural deformations and structural deformations change flow domain boundaries, a fully coupled, fluid-structure interaction finite element analysis is applied here. The throat segment or the elastic membrane is indicated by the heavy dark line. It is subjected to an external pressure. Unsteady flow is assumed at the entrance (left end); the fluid pressure at the downstream end (right end) is zero.

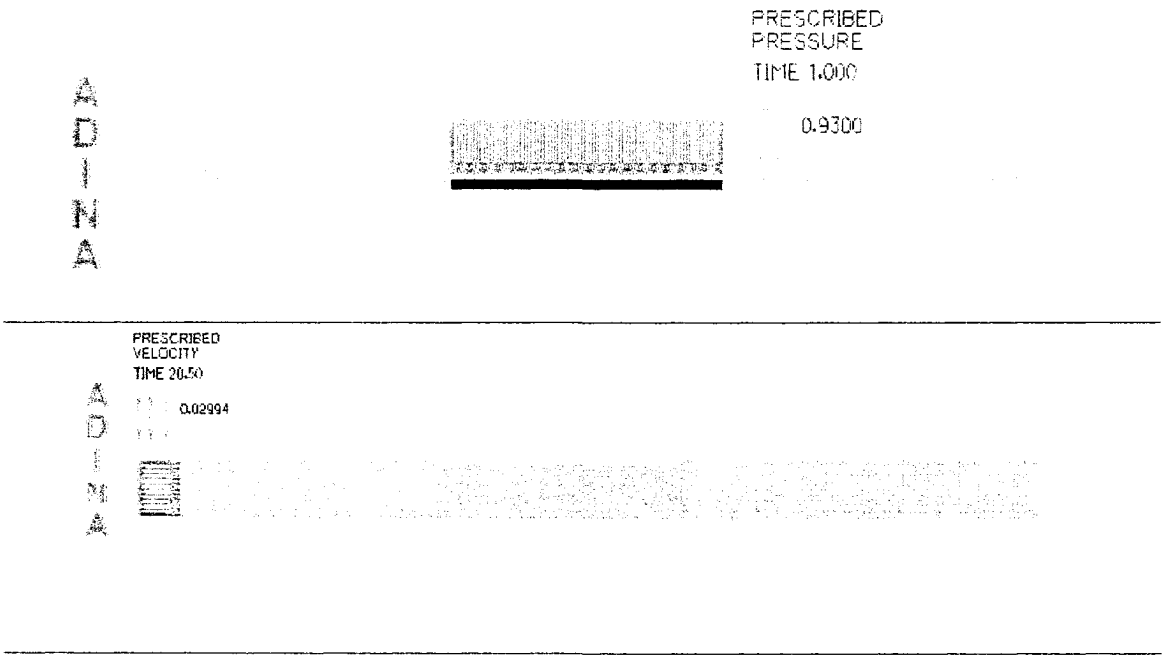

Figure A.9. The wall and fluid domain

The parameter values for the model are taken from (X.Y.Luo and T.J.Pedley, 1996-1998):

Entry length: $L_e = 0.05\ m$

Outlet length: $L_o = 0.07\ m$

Membrane length: $L_o = 0.05\ m$

Channel height: $H = 0.01\ m$

Channel width: $B = 0.01\ m$

Membrane thickness: $t = 0.001\ m$

Dynamic viscosity: $\mu = 0.001$ Pa s

Fluid density: $\rho_f = 1000\ \text{kg}/m^3$

Reynolds number: $\text{Re} = 300$

The following assumptions are made:

- The flow is unsteady and laminar.
- The fluid is incompressible, Newtonian and viscous.

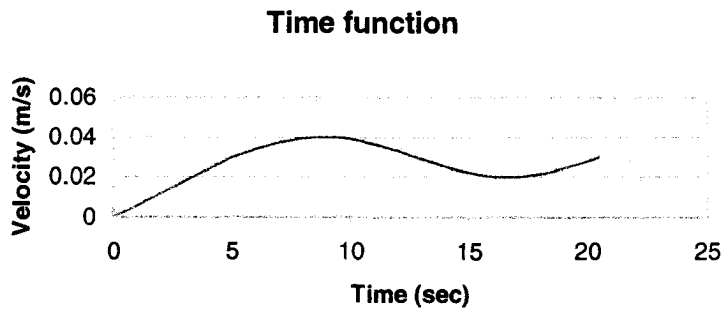

Figure A.10. Time function

A.4.3 ADINA results

A.4.3.1 Velocity profiles

Figure A.11 shows plots of velocity profiles along the channel axis at different time. The maximum velocity occurs at the throat. This high velocity causes high shear stress at the membrane.

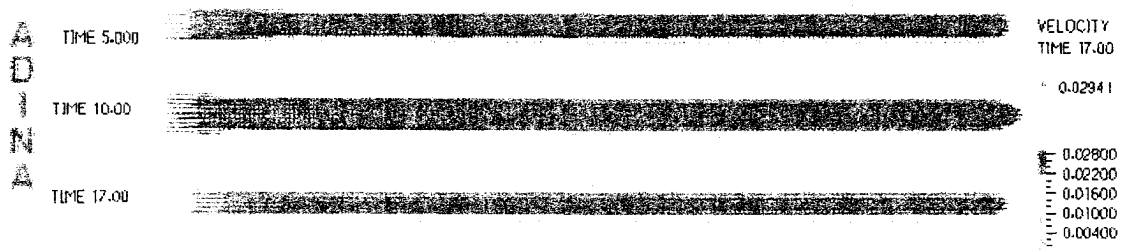

Figure A.11. Axial velocity profile at different time steps

A.4.3.2 Wall deformations

Figure A.12 shows the wall shape at different time instants. It can be seen that the position of maximum deformation changes with the time. Figure A.13 and A.14 show the

velocity of the wall in the axial direction at different time instants. It can be seen that the membrane oscillates in the axial direction, i.e., expansion and contraction.

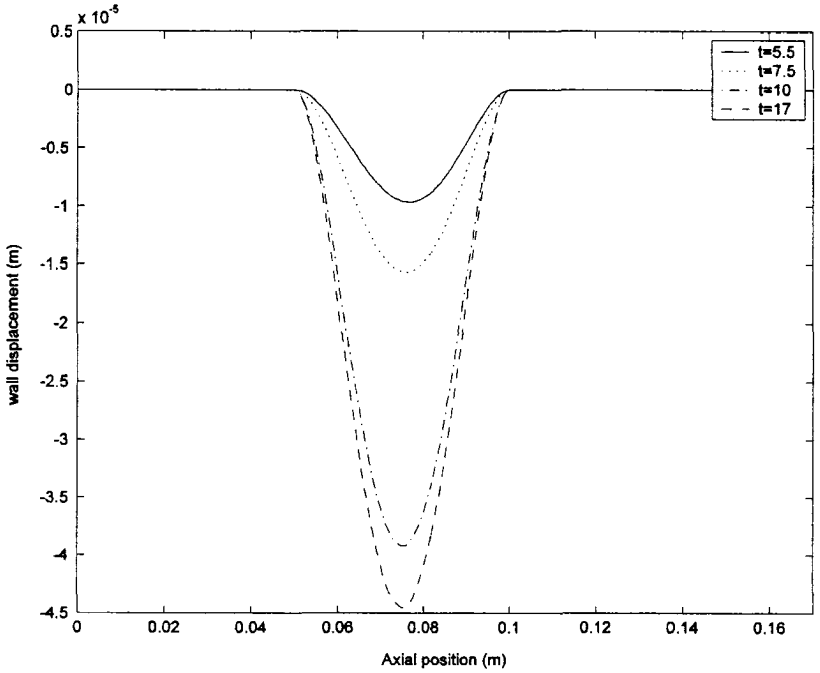

Figure A.12. Wall displacement at different time instants

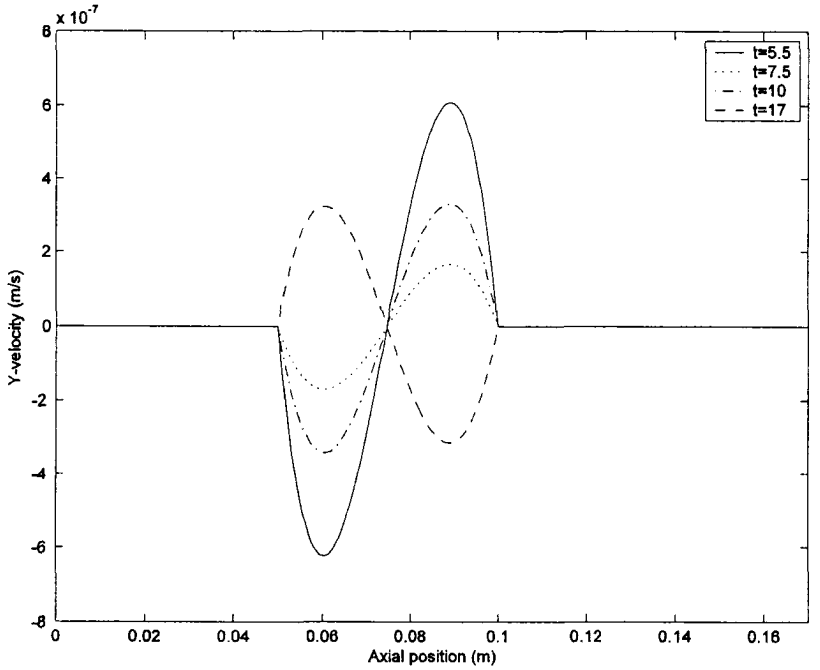

Figure A.13. Y- axial velocity at different time instants

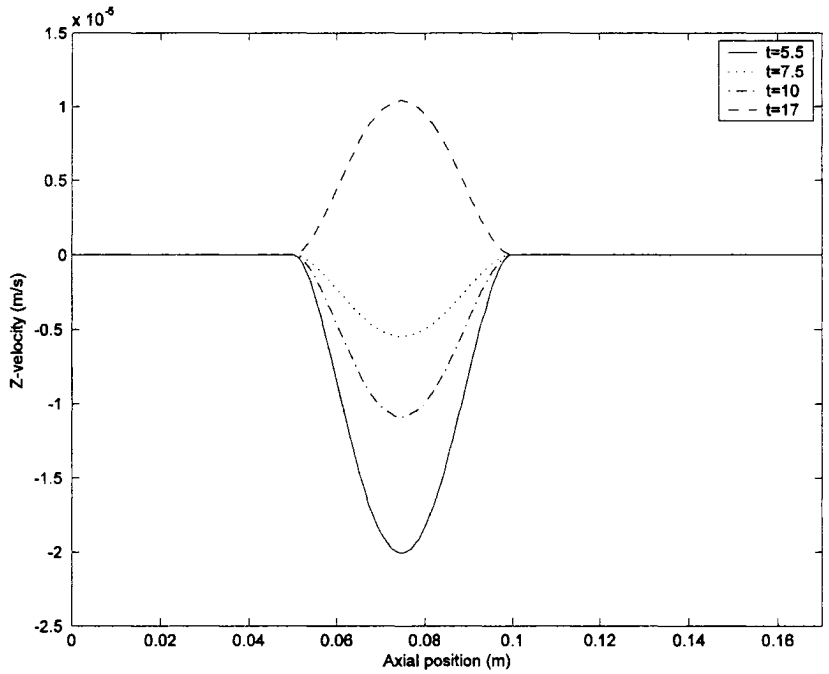

Figure A.14 Z- axial velocity at different time instants

Figure A.15 shows the membrane deformation vs. time at three axial locations. Note that the deformation starts from the minimum (at $t = 5$ second) to the maximum (at about $t = 14$ second), back to the minimum (at the end of the pulse).

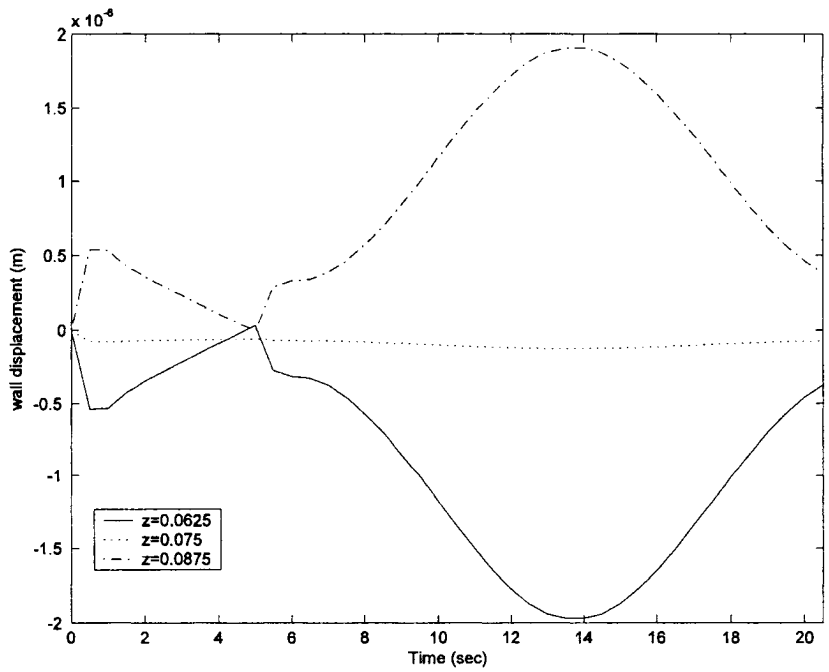

Figure A.15. Time variation of membrane for $f_e = 0.0215$, $U_a = 0.33$

A.4.3.3 Pressure field

Figure A.16 shows contour plots of pressure field at different time step.

Figure A.17 shows pressure distribution across the upper boundary (rigid wall and membrane) for different time instants.

Figure A.18 shows pressure distribution across the bottom boundary (rigid wall and membrane) for different time instants.

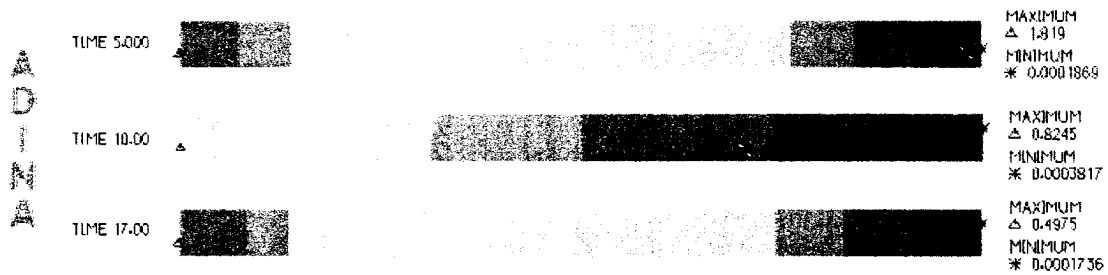

Figure A-16 Pressure distribution along the channel axis

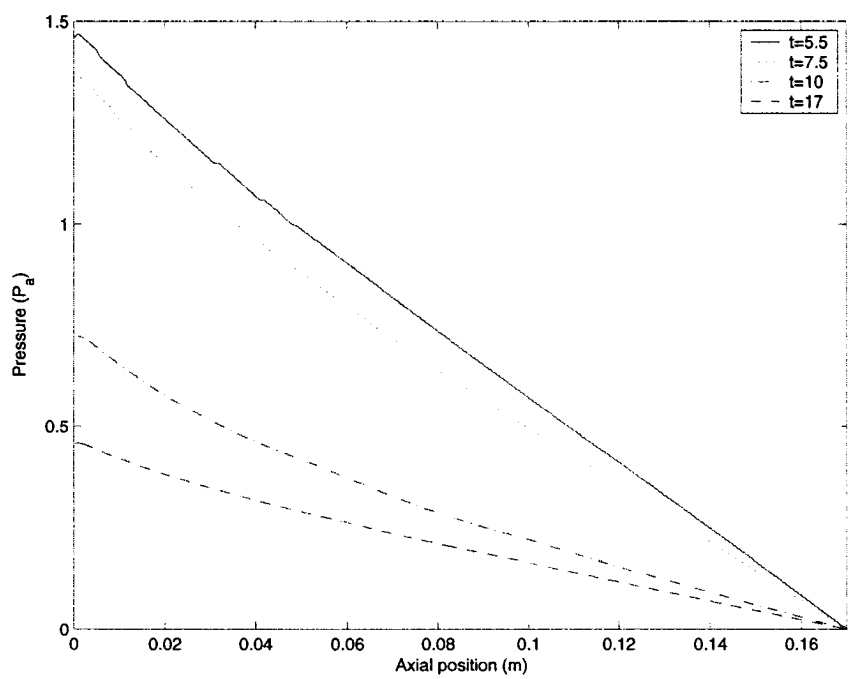

Figure A-17 Pressure distribution across the upper boundary

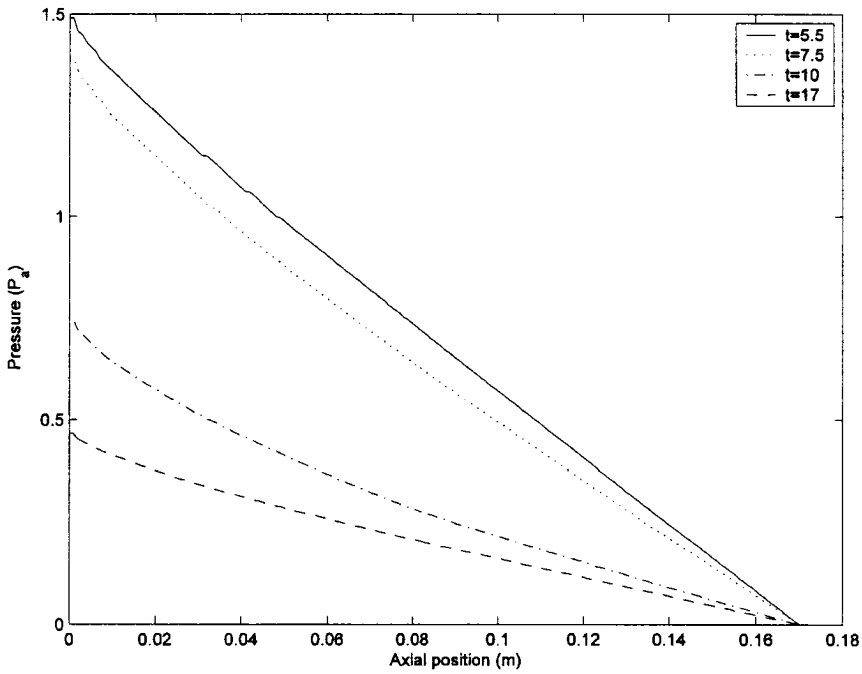

Figure A-18 Pressure distribution across the bottom boundary

A.4.3.4 Wall Principal stress and shear stress

The maximum wall principal stress and wall shear stress at different time instants are given in Figure A-19 and A-20. The maxima occurred at the junctions of the elastic membrane. Plaque cap rupture may be induced by such shear stress and cyclic compressive stresses.

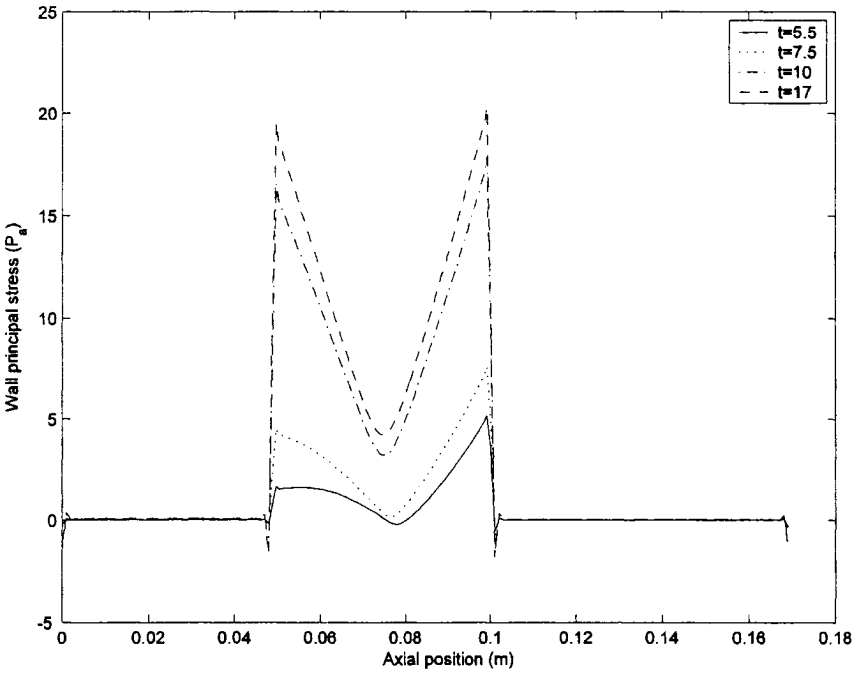

Figure A-19 Wall principal stress

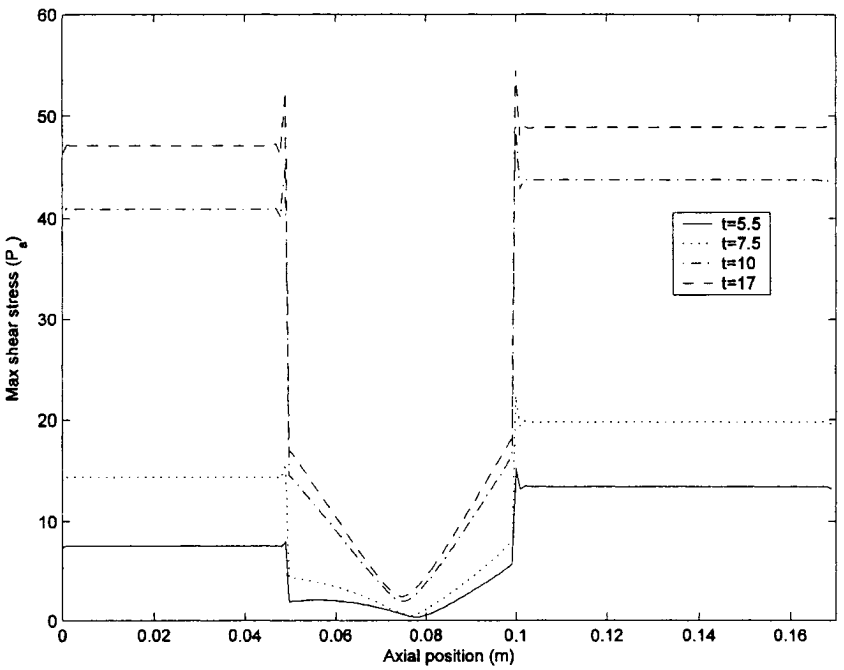

Figure A-20 Wall shear stress